In vivo characterization of the optical and hemodynamic properties of the human sternocleidomastoid muscle through ultrasound-guided hybrid near-infrared spectroscopies

Cortese, Lorenzo; Esteberena, Pablo Fernández; Zanoletti, Marta; Presti, Giuseppe Lo; Velazquez, Gloria Aranda; Janer, Sabina Ruiz; Buttafava, Mauro; Renna, Marco; Sieno, Laura Di; Tosi, Alberto; Mora, Alberto Dalla; Wojtkiewicz, Stanislaw; Dehghani, Hamid; Fraguier, Sixte de; Nguyen-Dinh, An; Rosinski, Bogdan; Weigel, Udo M.; Mesquida, Jaume; Squarcia, Mattia; Hanzu, Felicia A.

DOI:
10.1088/1361-6579/ad133a

Document Version
Publisher's PDF, also known as Version of record

Citation for published version (Harvard):
Cortese, L, Esteberena, PF, Zanoletti, M, Presti, GL, Velazquez, GA, Janer, SR, Buttafava, M, Renna, M, Sieno, LD, Tosi, A, Mora, AD, Wojtkiewicz, S, Dehghani, H, Fraguier, SD, Nguyen-Dinh, A, Rosinski, B, Weigel, UM, Mesquida, J, Squarcia, M, Hanzu, FA, Contini, D, Porta, MM & Durduran, T 2023, 'In vivo characterization of the optical and hemodynamic properties of the human sternocleidomastoid muscle through ultrasound-guided hybrid near-infrared spectroscopies', *Physiological Measurement*, vol. 44, no. 12, ad133a. https://doi.org/10.1088/1361-6579/ad133a

Physiological Measurement

PAPER • **OPEN ACCESS**

In vivo characterization of the optical and hemodynamic properties of the human sternocleidomastoid muscle through ultrasound-guided hybrid near-infrared spectroscopies

To cite this article: Lorenzo Cortese *et al* 2023 *Physiol. Meas.* **44** 125010

IOP Publishing Physiol. Meas. 44 (2023) 125010 https://doi.org/10.1088/1361-6579/ad133a

Physiological Measurement

IPEM Institute of Physics and Engineering in Medicine

OPEN ACCESS

RECEIVED
13 June 2023

REVISED
25 October 2023

ACCEPTED FOR PUBLICATION
7 December 2023

PUBLISHED
26 December 2023

PAPER

In vivo characterization of the optical and hemodynamic properties of the human sternocleidomastoid muscle through ultrasound-guided hybrid near-infrared spectroscopies

Lorenzo Cortese[1,*], Pablo Fernández Esteberena[1], Marta Zanoletti[1,2], Giuseppe Lo Presti[1], Gloria Aranda Velazquez[3], Sabina Ruiz Janer[3], Mauro Buttafava[4,5], Marco Renna[4,6], Laura Di Sieno[2], Alberto Tosi[4], Alberto Dalla Mora[2], Stanislaw Wojtkiewicz[7,8], Hamid Dehghani[7], Sixte de Fraguier[9], An Nguyen-Dinh[10], Bogdan Rosinski[10], Udo M Weigel[11], Jaume Mesquida[12], Mattia Squarcia[3,13], Felicia A Hanzu[3,14,15], Davide Contini[2], Mireia Mora Porta[3,14,15] and Turgut Durduran[1,16]

[1] ICFO—Institut de Ciències Fotòniques, The Barcelona Institute of Science and Technology, E-08860 Castelldefels (Barcelona), Spain
[2] Politecnico di Milano, Dipartimento di Fisica, I-20133 Milano, Italy
[3] IDIBAPS, Fundació Clínic per la Recerca Biomèdica, E-08036 Barcelona, Spain
[4] Politecnico di Milano, Dipartimento di Elettronica Informazione e Bioingegneria, I-20133 Milano, Italy
[5] Now at PIONIRS s.r.l., I-20124 Milano, Italy
[6] Now at Athinoula A. Martinos Center for Biomedical Imaging, MGH, Harvard Medical School, Charlestown, MA 02129, United States of America
[7] University of Birmingham, School of Computer Science, Edgbaston, Birmingham, B15 2TT, United Kingdom
[8] Now at Nalecz Institute of Biocybernetics and Biomedical Engineering, 02-109 Warsaw, Poland
[9] IMV Imaging, F-16000 Angoulême, France
[10] VERMON S.A., F-37000 Tours, France
[11] HemoPhotonics S.L., E-08860 Castelldefels (Barcelona), Spain
[12] Área de Críticos, Parc Taulí Hospital Universitari, E-08208 Sabadell, Spain
[13] Neuroradiology Department, Hospital Clínic of Barcelona, E-08036 Barcelona, Spain
[14] Endocrinology and Nutrition Department, Hospital Clínic of Barcelona, E-08036 Barcelona, Spain
[15] Centro de Investigación Biomédica en Red Diabetes y Enfermedades Metabólicas Asociadas (CIBERDEM), E-28029 Madrid, Spain
[16] Institució Catalana de Recerca i Estudis Avançats (ICREA), E-08010 Barcelona, Spain
[*] Author to whom any correspondence should be addressed.

E-mail: lorenzo.cortese@icfo.eu

Keywords: near-infrared spectroscopy, diffuse correlation spectroscopy, time-domain near-infrared diffuse optical spectroscopy, multi-modal imaging, ultrasound-guided hemodynamic monitoring, sternocleidomastoid muscle, mechanical ventilation

Abstract

Objective. In this paper, we present a detailed *in vivo* characterization of the optical and hemodynamic properties of the human sternocleidomastoid muscle (SCM), obtained through ultrasound-guided near-infrared time-domain and diffuse correlation spectroscopies. *Approach.* A total of sixty-five subjects (forty-nine females, sixteen males) among healthy volunteers and thyroid nodule patients have been recruited for the study. Their SCM hemodynamic (oxy-, deoxy- and total hemoglobin concentrations, blood flow, blood oxygen saturation and metabolic rate of oxygen extraction) and optical properties (wavelength dependent absorption and reduced scattering coefficients) have been measured by the use of a novel hybrid device combining in a single unit time-domain near-infrared spectroscopy, diffuse correlation spectroscopy and simultaneous ultrasound imaging. *Main results.* We provide detailed tables of the results related to SCM baseline (i.e. muscle at rest) properties, and reveal significant differences on the measured parameters due to variables such as side of the neck, sex, age, body mass index, depth and thickness of the muscle, allowing future clinical studies to take into account such dependencies. *Significance.* The non-invasive monitoring of the hemodynamics and metabolism of the sternocleidomastoid muscle during respiration became a topic of increased interest partially due to the increased use of mechanical ventilation during the COVID-19 pandemic. Near-infrared diffuse optical spectroscopies were proposed as potential practical monitors of increased recruitment of SCM during respiratory distress. They can provide clinically relevant information on the degree of the patient's respiratory effort that is needed to maintain an optimal minute ventilation,

with potential clinical application ranging from evaluating chronic pulmonary diseases to more acute settings, such as acute respiratory failure, or to determine the readiness to wean from invasive mechanical ventilation.

1. Introduction

The sternocleidomastoid muscle (SCM) is a superficial muscle laying obliquely at both sides of the neck, connecting the manubrium and the clavicle to the mastoid (Gray and Carter 1901). The contraction and the extension of this muscle allow, as a primary function, the rotation of the head and the flexion of the neck. Apart from assisting the movement of neck and head, the SCM has the function of being one of the accessory respiratory muscles to support the respiration in situations of increased respiratory volume and respiratory distress (Roussos and Macklem *et al* 1982).

Even before the COVID-19 pandemic brought the difficulties of mechanical respiration to worldwide attention, and, inspired by the SCM's role as a supporting muscle in respiration, a series of newer studies have stressed the importance of monitoring the SCM activity in cases of patients with severe respiratory distress. One marker of increased SCM activity, as in other muscles, are the hemodynamic alterations which have been proposed as predictors of ventilatory failure in case of chronic pulmonary diseases, such as chronic obstructive pulmonary disease (COPD) (Guenette *et al* 2011, Shadgan *et al* 2011, Katayama *et al* 2015, Basoudan *et al* 2016, Reid *et al* 2016, Tanaka *et al* 2018, Rodrigues *et al* 2020). Also, in more acute settings such as acute respiratory failure, SCM activity alterations are hypothesized to provide information to determine the need for initiating mechanical respiratory support, or to decide whether the ventilator support is no longer needed (Reid *et al* 2016, Istfan *et al* 2021, Gømez *et al* 2023). This could impact healthcare given the limitations of current methodologies driving such clinical decisions (Meade *et al* 2001, Funk *et al* 2010).

In this framework, near-infrared diffuse optical technologies (Durduran *et al* 2010) have the potential to play a role in real-time monitoring of the SCM activity as non-invasive methods to quantify quantify the local tissue hemodynamics at the microvascular level, by probing the deep tissue (1–3 cm) using near-infrared (600–1100 nm) light (Istfan *et al* 2021).

Among the different near-infrared spectroscopic technologies, time-domain near-infrared spectroscopy (TD-NIRS, also known as time-resolved near-infrared spectroscopy, TRS) (Patterson *et al* 1989, Pifferi *et al* 2016) is emerging as a reliable and practical tool to measure microvascular tissue/blood oxygenation. TD-NIRS proposes an improvement in accuracy and precision over the continuous-wave near-infrared spectroscopy (CW-NIRS) that is clinically accepted (Ferrari *et al* 2004, Wolf *et al* 2007, Murkin and Arango 2009, Torricelli *et al* 2014, Yamada *et al* 2019). It works by injecting short laser pulses in the tissue and detecting the diffused signal in a time-resolved manner. Therefore, TD-NIRS is able to measure absolute, wavelength-dependent absorption and scattering coefficients, providing a more robust and reliable determination of absolute oxy-, deoxy- and total hemoglobin concentrations (HbO_2, Hb and THC), and local tissue/blood oxygen saturation (StO_2). TD-NIRS techniques are used since decades in clinical studies, and the reliability of TD-NIRS devices is commonly tested through standardized multi-laboratory accepted protocols, validating device precision, accuracy and other performances under different conditions (Pifferi *et al* 2005, Wabnitz *et al* 2014a, 2014b, Pifferi *et al* 2015, Lanka *et al* 2022).

Diffuse correlation spectroscopy (DCS) (Boas and Yodh 1997, Yu *et al* 2007, Durduran *et al* 2010) on the other hand measures the fluctuations of laser speckle intensity due to light scattering by moving red blood cells after injecting coherent light in the tissue. By utilizing the appropriate physical model, DCS allows the quantification of the tissue microvascular blood flow (i.e. blood flow index, BFi). As a rapidly emerging clinical technique, DCS has been extensively used in the last 10–15 years for studying muscle hemodynamics (Durduran *et al* 2010, Yu 2012a). The effectiveness of DCS in monitoring blood flow in muscles has been validated in different ways and conditions, and compared to different techniques as ASL-MR and Doppler ultrasound (Yu *et al* 2007, Li *et al* 2015, Bangalore-Yogananda *et al* 2018).

The combination of DCS and NIRS technology such as TD-NIRS, CW-NIRS or frequency domain NIRS (FD-NIRS), allows to retrieve complementary information about tissue hemodynamics, composition and structure, and also, to obtain information about tissue oxygen metabolism, that is, the metabolic rate of oxygen extraction (MRO_2) relating the effective oxygen delivery and consumption by the local tissue (Durduran *et al* 2010, Durduran and Yodh 2014). During the recent years, the combination of these complementary techniques has been used successfully in several clinical and preclinical studies involving a wide range of situations, from cancer diagnosis and therapy follow-up, to brain monitoring (Cheung *et al* 2001, Culver *et al* 2003, Durduran *et al* 2004, Zhou *et al* 2007, Roche-Labarbe *et al* 2010, Choe and Durduran 2011, Yu 2012b, Roche-Labarbe *et al* 2012, Verdecchia *et al* 2013, Buckley *et al* 2014, Lindner *et al* 2016, He *et al* 2018, Giovannella *et al* 2019, Quaresima *et al* 2019, Milej *et al* 2020).

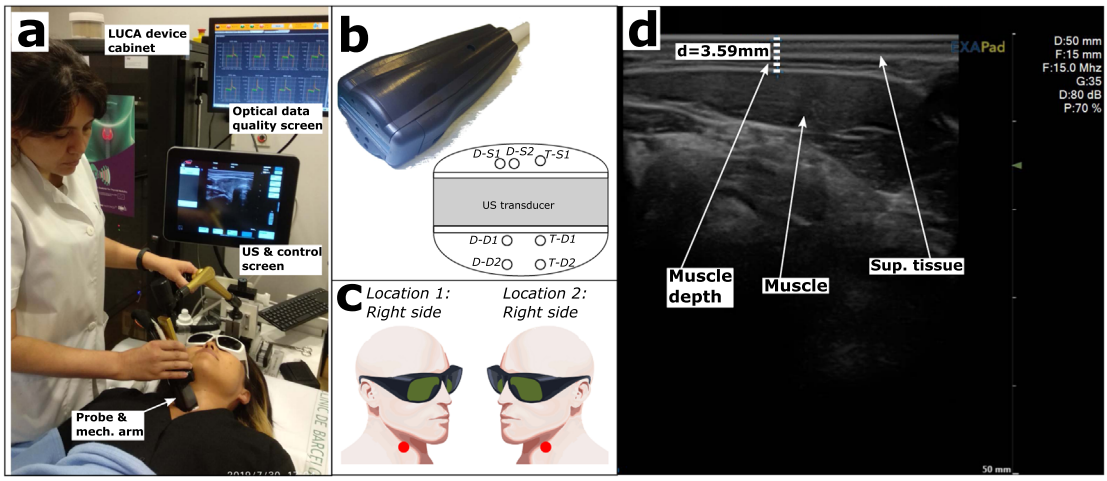

Figure 1. (a) Picture of the measurement procedure, with US-guided probe placement. (b) Picture of the multi-modal US-optical probe; center: fiber tips configuration at the probe nose (DCS sources: D-S1 and D-S2; DCS detectors: D-D1 and D-D2, short and long SDSs respectively; TD-NIRS source: T-S1; TD-NIRS detectors: T-D1 and T-D2, short and long SDSs respectively). Adapted with permission from Cortese *et al* (2021a)© The Optical Society. (c) measurement locations. (d) Example of US image of the SCM region acquired simultaneously with the optical data. In the picture, we have highlighted the different tissues, i.e. muscle and superficial (sup.) tissue, composed by skin, adipose tissue and fascia, and the depth of the muscle. Further details and images of the experimental setup are reported in Cortese *et al* (2021a).

Differently to all the previous NIRS studies on the human sternocleidomastoid muscle (Guenette *et al* 2011, Shadgan *et al* 2011, Katayama *et al* 2015, Basoudan *et al* 2016, Reid *et al* 2016, Tanaka *et al* 2018, Rodrigues *et al* 2020, Istfan *et al* 2021), here we have employed a unique multi-modal device combining ultrasound (US) imaging with TD-NIRS and DCS (Cortese *et al* 2021a) to characterize the SCM of a group of healthy subjects and thyroid nodule patients. This multi-modal approach allowed a more reliable, precise and accurate determination of the optical and hemodynamic properties of such muscle, providing simultaneous information about tissue anatomy, oxygenation, perfusion and oxygen metabolism, and enabling also improved precision of the optical measurement due to US guidance.

2. Materials and methods

2.1. Experimental setup: multi-modal US-guided hemodynamic monitor

A multi-modal hybrid platform combining time-domain near-infrared spectroscopy, diffuse correlation spectroscopy and clinical ultrasound has been used for the measurement campaign. A picture of the device, during the measurement procedure, is reported in figure 1(a). The device description and its validation in laboratory and clinical settings have been previously reported in detail in Cortese *et al* (2021a).

Briefly, the TD-NIRS module (Renna *et al* 2019) is composed by a custom-made eight wavelength pulsed laser system in the wavelength range 635−1050 nm. The DCS module (Cortese *et al* 2021b) consists of a long coherence single longitudinal mode continuous-wave laser at 785 nm and sixteen detection channels. The ultrasound system is a customized commercial device (EXAPad, IMV Imaging, France) which is currently commercialized by Quantel Medical (France) under the EvoTouch+ product brand.

The different technologies are integrated in a single device through a dedicated control module (custom product, HemoPhotonics S.L., Spain) while the simultaneous acquisition of TD-NIRS, DCS and US signals are allowed by a multi-modal optical/US probe (Cortese *et al* 2021a). This probe (custom product, Vermon SA, France), reported in figure 1 (b), includes an ultrasound transducer (10.6 MHz center frequency) and source and detector fibers for TD-NIRS and DCS. Both TD-NIRS and DCS have two different source-detector fiber configurations: (i) long source-detector separation (long SDS), where source and detection fiber tips are separated by 2.5 cm, and (ii) short source-detection separation (short SDS), where source and detection fiber tips are separated by 1.9 cm.

The multi-modal method utilized in this study, combining DCS, TD-NIRS and US imaging, has several benefits. DCS and TD-NIRS provide complementary information about different aspects of tissue hemodynamics, and their combination allows to retrieve information about oxygen metabolism. Additionally, simultaneous US imaging better allow the guidance of the optical measurement, assuring a more reliable probe placement, improving the spatial resolution and measurement reproducibility.

2.2. Study population and protocol of measurement

The data reported in this paper consist of a retrospective analysis of measurements acquired in the context of a larger study, with focus on thyroid nodule hemodynamics (LUCA-project, http://www.luca-project.eu). In this framework, the signal from the sternocleidomastoid muscle has been acquired as a reference to establish whether the thyroid hemodynamics differ from the overlaying and surrounding muscle. The *in vivo* measurement campaign has been conducted according to the guidelines of the Declaration of Helsinki, and following the SAGER (Sex and Gender Equity in Research) guidelines for reporting sex/gender information. The study has been approved by Hospital Clínic Barcelona local Ethic Committee and Agencia Española de Medicamentos y Productos Sanitarios (AEMPS). Before starting the measurement sessions, all the subjects have been asked to provide written informed consent. Various demographic parameters were also acquired such as biological sex (self reported), age, height, weight, and body mass index (BMI).

Two cohorts of subjects, healthy controls and thyroid nodule patients, have been recruited. In order to classify the subjects into these two groups, all subjects have also undergone a blood analysis and a clinical ultrasound examination. Female subjects during their menstrual period have been excluded from both groups because of possible hemodynamic alterations. The healthy controls have been assumed to be without any thyroid pathologies, with a normal thyroid function, with a negative autoimmunity, and with a normal thyroid ultrasound image. The patient group has been recruited from subjects diagnosed with nodular thyroid pathologies who are scheduled to undergo surgery including patients with benign nodules, malignant nodules and multinodular goiter. The particular thyroid conditions are not direct particular interest to this study, and all the nodule patients included in the study have a normal thyroid function. In any case, we have decided to report the results since thyroid pathologies are very common in the general population and if the SCM hemodynamics and optical properties are altered due to the pathology, they should be taken into account.

The measurements have been performed with the subject laying supine, with the neck slightly hyper-extended in straight (not lateralized) position (see figure 1(a)). For eye safety, patients have been asked to wear laser-safety goggles. The multi-modal probe was placed on the subject skin by using an opaque lotion (Polysonic Ultrasound Lotion, Parker, US), which allows ultrasound coupling without affecting the optical acquisitions, as reported in Di Sieno *et al* (2019). With the guidance of the US real-time images, the correct position over the sternocleidomastoid muscle, just next to the side of the corresponding thyroid lobe, has been found, and lastly, the probe was fixed through a mechanical arm to reduce artifacts due to movements during the data acquisition.

The concurrent US imaging has allowed not only the correct, repeatable placement of the probe but also the determination of the depth of the sternocleidomastoid muscle, i.e. the thickness of the overlaying adipose tissue layer. For all the subjects, two different locations, that is, left and right sternocleidomastoid muscle, have been measured (see figure 1 (c)). The duration of each acquisition (consisting of DCS and TD-NIRS data and simultaneous US images) was approximately 100 s, and two acquisitions per location, separated by approximately 10 min, have been repeated, with a sequence of measurements consisting of location 1—location 2—location 1 (second repetition) - location 2 (second repetition)[17]. The starting location, left versus right has been randomized to avoid possible drifts due to systematic physiological changes during the procedure

2.3. Optical data analysis

The reduced scattering coefficient μ_s' and absorption coefficient μ_a at different wavelengths have been obtained from the TD-NIRS acquisitions by fitting of the solution of the diffusion equation for a semi-infinite homogeneous medium (Haskell *et al* 1994, Contini *et al* 1997) after convolving this solution with the instrument response function (IRF). In the fitting procedure, the μ_s' at different wavelengths λ has been constrained by the empirical Mie relation $\mu_s'(\lambda) = A \cdot (\lambda/\lambda_0)^{-b}$, where λ_0 is the reference wavelength ($\lambda_0 = 785$ nm), A is the estimated reduced scattering coefficient at 785 nm, and b is the so-called scattering power (Mourant *et al* 1997, Pogue *et al* 2001, Srinivasan *et al* 2003, DAndrea *et al* 2006, Cortese *et al* 2018).

Since it is of interest for other near-infrared spectroscopy modalities, the differential pathlength factors DPF, have been calculated by using the formula $\mathrm{DPF}(\lambda) \cong (1/\rho) \cdot (c/n) \cdot t(\lambda)$ (Delpy *et al* 1988, Pirovano *et al* 2021), where ρ is the source-detector fiber tip distance, c the speed of light, n the refractive index of the tissue (we set $n = 1.4$ independently from the wavelength (Bolin *et al* 1989, Durduran *et al* 2010, Ciarrocchi and Belcari 2017)), and $t(\lambda)$ is the photon mean time-of-flight, defined as the first moment of the measured distribution of the time of flights (DTOF).

[17] As previously reported, these measurements are part of a larger study on thyroid nodule hemodynamics. In this respect, the original protocol also included measurements on the corresponding thyroid lobe before each muscle acquisition.

The retrieved μ_s' and μ_a values have been then used as input parameters to retrieve the blood flow index (BFi) from DCS data by fitting the acquired photon intensity autocorrelation curves with the solution of the electric field correlation diffusion equation for a semi-infinite homogeneous medium (Durduran *et al* 2010).

The concentrations of oxy- and deoxy-hemoglobin (HbO_2 and Hb, respectively)[18] have been obtained by assuming linearity between the absorption coefficients at different wavelengths and the chromophore concentrations (i.e. HbO_2 and Hb), through the relation $\mu_a = \sum_i \epsilon_i(\lambda) \cdot c_i$, where c_i is the concentration of the i-th chromophore and ϵ_i its extinction coefficient (Durduran *et al* 2010). In the inversion procedure, the absorption coefficients at three wavelengths, 669 nm, 722 nm and 825 nm, have been used. Even though additional wavelengths of the device could be used to recover a more quantitative measure, for simplicity and to avoid confounding the results with errors from additional variables, the water concentration was fixed to 78%, and, for the wavelengths used in the analysis, lipid contribution to NIRS signal was considered negligible (Lindner *et al* 2016). Finally, the total hemoglobin concentration and the tissue oxygen saturation were obtained through the relations $THC = HbO_2 + Hb$ and $StO_2 = HbO_2/THC$. We note here that a future study could allow to utilize the additional wavelengths in this device, that go beyond the typically utilized range, for the determination of additional chromophores and a better compensation of the myoglobin and hemoglobin signals.

In addition, by combining the hemodynamic parameters obtained from DCS and TD-NIRS data, the local tissue oxygen metabolism, that is, the metabolic rate of oxygen extraction MRO_2 has been quantified, by using the relation $MRO_2 = BFi \cdot CaO_2 \cdot OEF$. Here the product of BFi with the arterial oxygen concentration CaO_2 represents the availability of oxygenated blood per unit time. The oxygen extraction fraction (*OEF*) represents the fraction of blood oxygen consumed by the tissue (Durduran *et al* 2010). Assuming a compartmentalized model, under steady-state balance, the oxygen extraction fraction can be written as $OEF = (SaO_2 - StO_2)/(\gamma \cdot SaO_2)$, where SaO_2 is the arterial oxygen saturation and γ is the fraction of venous blood volume (including venule and capillary compartments). Thus, $MRO_2 = BFi \cdot \frac{1}{\gamma}(SaO_2 - StO_2) \cdot k \cdot CHb_{blood}$ (Culver *et al* 2003), where $k = 1.36$ ml g^{-1} is the volume of O_2 per unit mass of hemoglobin for mammals (Larimer 1959) and CHb_{blood} is the total hemoglobin concentration in blood. The value for γ cannot be estimated for each subject, so the variable used for all following statistical analysis is the combination γMRO_2 with units of cm^2/s (same as BFi). In turn, CHb_{blood} values have been measured in blood tests obtained previous to the measurement protocol and, as all subjects were healthy as far SaO_2 is concerned, the mean value over all the population ($98\% \pm 1\%$) has been considered.

For all the optically-derived parameters, we have evaluated and compared the precision of a single acquisition, the reproducibility over probe repositioning on the same location, and the whole population variability, by calculating the coefficient of variation defined as $CV = 100 \cdot \sigma(x)/\langle x \rangle$, where $\sigma(x)$ is the standard deviation and $\langle x \rangle$ the average of the variable under consideration (Cortese *et al* 2021c).

2.4. Statistical analysis

Experimental, demographic and anatomical parameters have been utilized to explore whether they are associated with the measured optical variables. This includes demographic variables as sex, age and BMI, anatomical considerations like the side of the neck, depth and thickness of the muscle, the thyroid pathologies as nodule presence and side, as well as the source-detector separation.

The statistical analysis has been conducted in R Statistical Software (v4.0.0, R Core Team 2020), using base packages and 'lme4' (v1.1.23) and 'performance' (v0.9.1) packages, and 'raincloud' package for plots (Allen *et al* 2021). The boxplots reported in section 3.2 detail the minimum and maximum values (excluding outliers), median, and first and third quartiles.

As a first step of the statistical analysis, the normality of the distributions has been checked by using the Shapiro-Wilk test on data averaged sequentially over the duration of the single measurement (approximately 100 s of data acquisition, see section 2.2), over repetitions for probe replacement and the side of the neck. This resulted in one value per patient. Then, correlations between demographic variables and anatomical information from US, have been tested by calculating the Pearson correlation coefficient.

In general, to test for significant effects of the different parameters on optical variables, linear mixed effects (LME) models have been used fitting a random value for each side of the neck and considering as the random-effect structure the probe replacement index nested within the subject id number. For the special case of testing for a difference between sides of the neck (and side relative to the nodule position), the sides have been not considered to have different random intercepts.

The demographic or anatomical parameter to be tested has been considered as a unique fixed effect in a separate model each time. This model was compared to a null model without the fixed effect through a

[18] Due to spectral congruence in the near-infrared region, NIRS technology is unable to distinguish between hemoglobin and myoglobin absorption, which contribution can be significant in skeletal muscles. In this paper, with the term 'hemoglobin', we intend the sum of hemoglobin and myoglobin, as commonly used in NIRS studies (Barstow 2019).

Table 1. Demographic table of the subjects included in the study, including parameters such as sex, the number N of subjects per group, the age, body mass index BMI, and the depth and thickness of the muscle (measured with US). For these parameters, the average value $\pm$ the standard deviation is reported, and in parenthesis the minimum and maximum values. Statistically significant differences in the demographic variables are highlighted with '*' for differences between healthy subject and nodule patients, and with '$\star$' for differences between males an females within the corresponding group.

	N	Age (years)	BMI (kg m^{-2})	Muscle depth (mm)	Muscle thickness (mm)
All	65	46(18, 70) $\pm$ 13	25(16.0, 35.5) $\pm$ 4	3.1(1.26, 6.06) $\pm$ 1.0	6.6(4.55, 11.10) $\pm$ 1.5
Males	16	48(27, 67) $\pm$ 12	26(20.1, 29.6) $\pm$ 3	3.0(1.38, 4.85) $\pm$ 0.9	$\star$7.7(4.76, 11.10) $\pm$ 1.9
Females	49	45(18, 70) $\pm$ 14	24(16.0, 35.5) $\pm$ 5	3.2(1.26, 6.06) $\pm$ 1.0	$\star$6.2(4.55, 8.03) $\pm$ 1.1
Healthy	17	*36(24, 49) $\pm$ 9	*23(17.5, 29.4) $\pm$ 3	*2.4(1.26, 4.05) $\pm$ 0.8	6.8(5.17, 9.07) $\pm$ 1.4
Males	6	38(27, 49) $\pm$ 8	$\star$25(20.1, 29.4) $\pm$ 3	2.4(1.38, 3.75) $\pm$ 0.7	$\star$7.7(6.18, 9.07) $\pm$ 1.3
Females	11	36(24, 49) $\pm$ 9	$\star$22(17.5, 28.7) $\pm$ 3	2.4(1.26, 4.05) $\pm$ 0.8	$\star$6.3(5.17, 7.36) $\pm$ 1.3
Patients	48	*49(18, 70) $\pm$ 13	*25(16.0, 35.5) $\pm$ 4	*3.4(1.93, 6.06) $\pm$ 1.0	6.5(4.55, 11.10) $\pm$ 1.5
Males	10	54(37, 67) $\pm$ 10	27(24.9, 29.6) $\pm$ 2	3.4(2.51, 4.85) $\pm$ 0.9	$\star$7.8(4.76, 11.10) $\pm$ 1.3
Females	38	48(18, 70) $\pm$ 14	25(16.0, 35.5) $\pm$ 5	3.4(1.93, 6.06) $\pm$ 1.0	$\star$6.2(4.55, 8.03) $\pm$ 1.1

likelihood ratio test with restricted maximum likelihood (REML) procedure. When the test yielded a significant difference between models ($p-$ value < 0.05), it has been refitted without REML to obtain unbiased estimates.

In addition, an exponential dependence of the optical and hemodynamic parameters on age, BMI and muscle depth has been tested with a LME model by considering the logarithm of the measured parameters, and the quality of the fit was compared to that of the linear model.

3. Results

3.1. Study population

The pertinent information about the population is reported in table 1. In total, sixty-five subjects (forty-nine females, sixteen males, average age 46 years, minimum age 18, maximum 70) have been included in the study. Among the included sixty-five subjects, seventeen are in the healthy subject group (eleven females, six males), and forty-eight in the thyroid nodule patient group (thirty-eight females, ten males). Statistically significant differences in the demographic variables are highlighted with '*' for differences between healthy subject and nodule patients, and with '$\star$' for differences between males and females within the corresponding group. Healthy subjects differ from thyroid nodule patients for age, BMI and average muscle depth. Males show a larger muscle thickness respect to females within all the groups considered. Within the healthy subject group, males show higher BMI. Lastly, the population of this study followed the epidemiological characteristics of thyroid nodules. Nodules are more common with increasing age and in women than in men (Hegedüs 2004, Cooper *et al* 2009, Kwong *et al* 2015).

3.2. Distribution of measured parameters and optical properties

In figure 2 we report the distributions of the measured variables, together with the boxplots, for both long and short SDSs, obtained considering one data point per subject (see above)[19] Detailed tables with the average values of the parameters considered are reported in appendix A. In table A3, we furthermore report the comparison between the variability of a single acquisition (precision of a single acquisition of approximately 100 s), between repetitions (due to probe repositioning on the same location), and the whole population variability, for the parameters reported in figure 2.

The normality of the distributions reported in figure 2 has been tested by using the Shapiro-Wilk test. We have found that parameter b is normally distributed for both source-detector separations, while μ_a at 669 nm is normally distributed only for the long SDS. The rest of parameters are not normally distributed. We note that the LME method that as employed for further statistics does not require normality (Schielzeth *et al* 2020, Knief and Forstmeier 2021). Figure 2 also highlights some possible differences between long and short SDSs acquisitions. The statistical tests applying the LME model shows significant differences between long and short SDSs for all the parameters measured, except for the μ_a at 669 nm. Details of these tests are shown in table B1 in appendix B, where we report the LME model best estimate (and standard error) of the measured value, highlighting the differences between the groups considered. As expected, the values resulting from fitting the LME model, only slightly differ from the mean values obtained considering one average point per subject, reported in appendix A.

[19] In case of non-dimensional or unitless variables, we have used the notation 'adim.'.

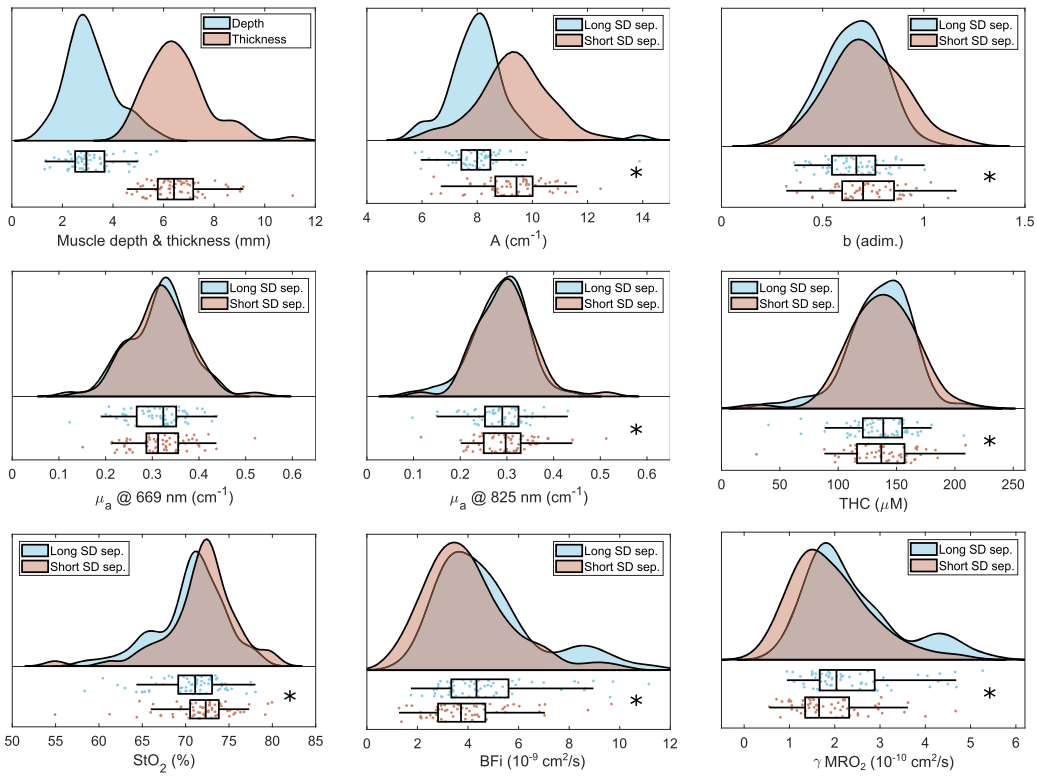

Figure 2. Distributions and boxplots of the derived parameters. Muscle depth and thickness have been measured through ultrasound imaging, while the other parameters have been derived by the optical measurements. Distributions and boxplots have been obtained considering one data point per subject ($N = 65$), result of the average over measurement duration, repetitions and locations (left and right muscle). Statistically significant differences between long and short SDS acquisitions are highlighted with an asterisk.

In the following section, we will focus on results only related to the longer SDS (2.5 cm) acquisitions, which, as discussed in section 4, is in first approximation more sensitive to the deeper tissue properties, that is, the sternocleidomastoid muscle.

A detailed characterization at different wavelengths of the optical properties, that is μ_s', μ_a and DPF determined by TD-NIRS acquisitions, is reported in figure 3 and in tables A4, A5 and A6 in appendix A. We note that these plots are for illustration purposes of the overall tendencies and the statistically significant differences should be checked by using the above-mentioned tables in appendix B.

3.3. Effects of measurement location and sex

The dependence of the measured parameters (for the long SDS) on the location (left versus right muscle), and on the subject biological sex, has been studied. In figures 4 and 5, we highlight the differences between the muscle location and the sex. In the figures, the parameters showing statistically significant differences are highlighted by reporting the LME model best estimate in red and by an asterisk, while the estimate of the parameters not showing significant differences are reported in light gray. Detailed results of the statistical tests are reported in tables B2 and B3 in appendix B.

3.4. Effect of age, BMI, muscle depth and thickness

In this study we have considered a population with age ranging from 18 to 70 years, with an average value of 46 . Considering such a wide range, we have analyzed the effects of this variable as confounding factor on the measured parameters. The correlations are shown in figure 6, where we report the data points of each subject, for the long SDS, together with the fitted lines in red where we have found statistically significant correlations. Detailed data of the statistical tests are reported in appendix B, table B4.

Moreover, as reported in section 2.4, we have tested whether an exponential relation better describes the dependence between the measured parameters on subject age, finding no improvements for any of the analyzed variables with respect to the linear model.

We also have studied the effects of body mass index, depth and thickness of the muscle (measured through simultaneous US imaging), on the measured parameters (for the long SDS). Such correlations have been

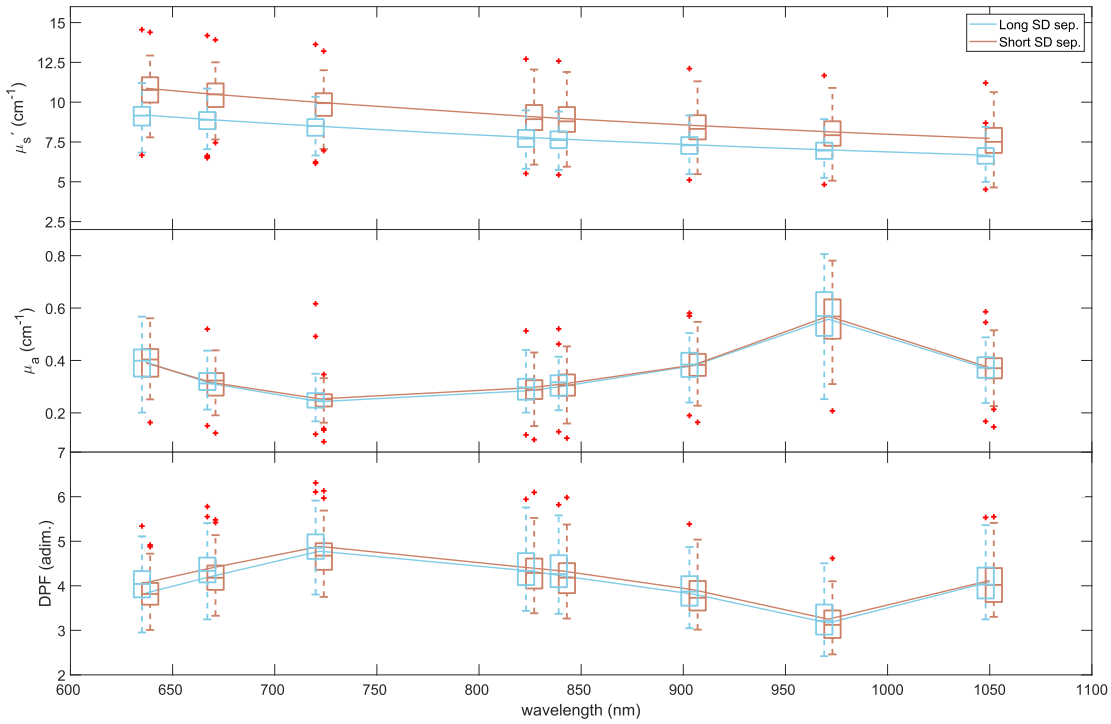

Figure 3. (Upper panel) The measured reduced scattering coefficient, (center panel) the absorption coefficient, and, (lower panel) differential pathlength factor of the sternocleidomastoid muscle over different wavelengths at both long and short SDSs is shown. The average over all subjects (solid lines) is shown together with a boxplot. Outliers are marked in red.

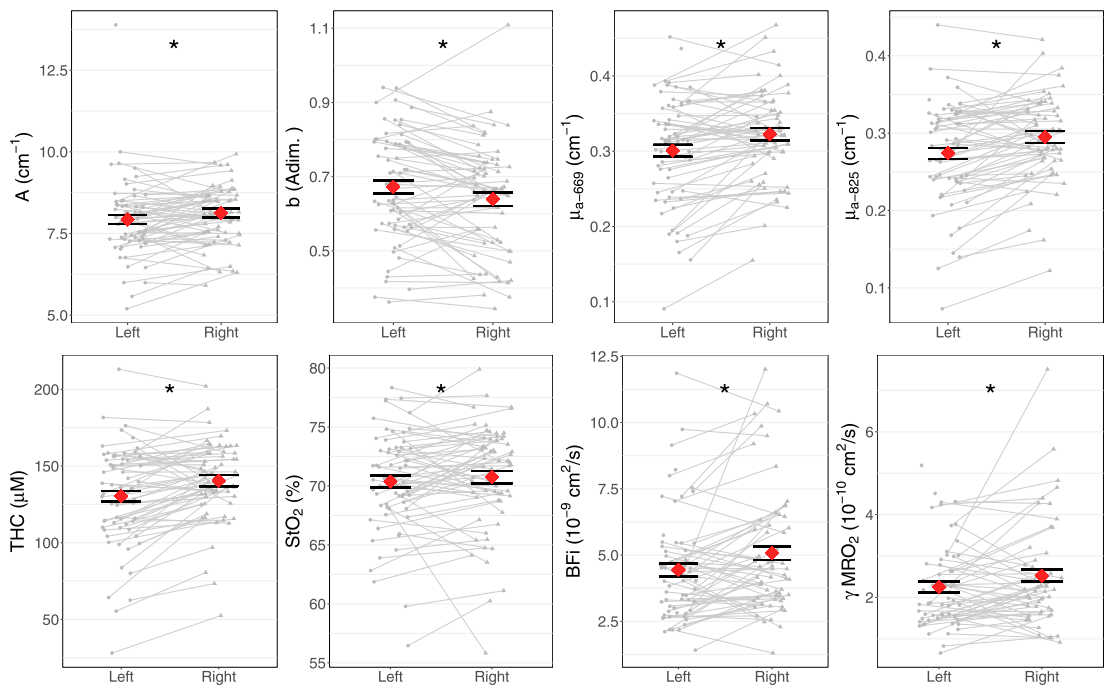

Figure 4. Differences between left (circle) and righ (triangle) is shown. The data points from the same subject are connected by the gray lines. LME model best estimates with error bars (standard error) are overlapped to data points, and are reported in red (and together with an asterisk) when differences between groups are statistically significant.

represented in figures 7 and 8 (plots not reported for muscle thickness), and the results of statistical tests reported in tables B5, B6 and B7. In case the exponential model better explains such correlations, such tables also report the logarithm of the parameter under consideration as independent variable.

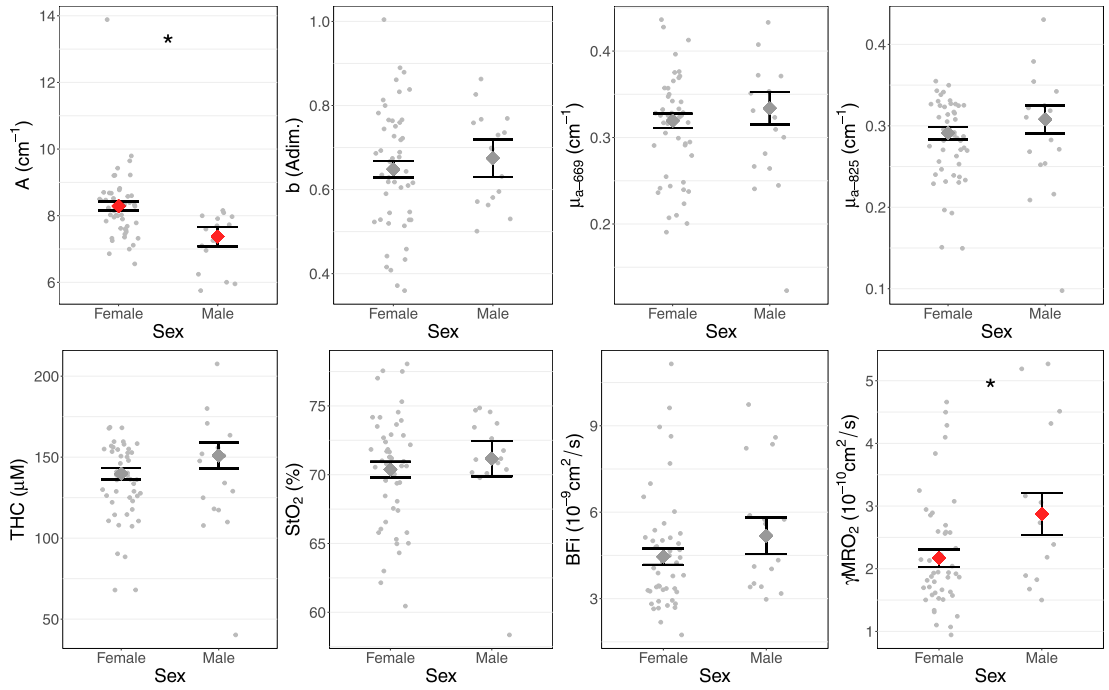

Figure 5. Differences between sexes is shown. The model best estimates with error bars are overlapped to data points, and are reported in red and highlighted with an asterisk when differences between groups are statistically significant.

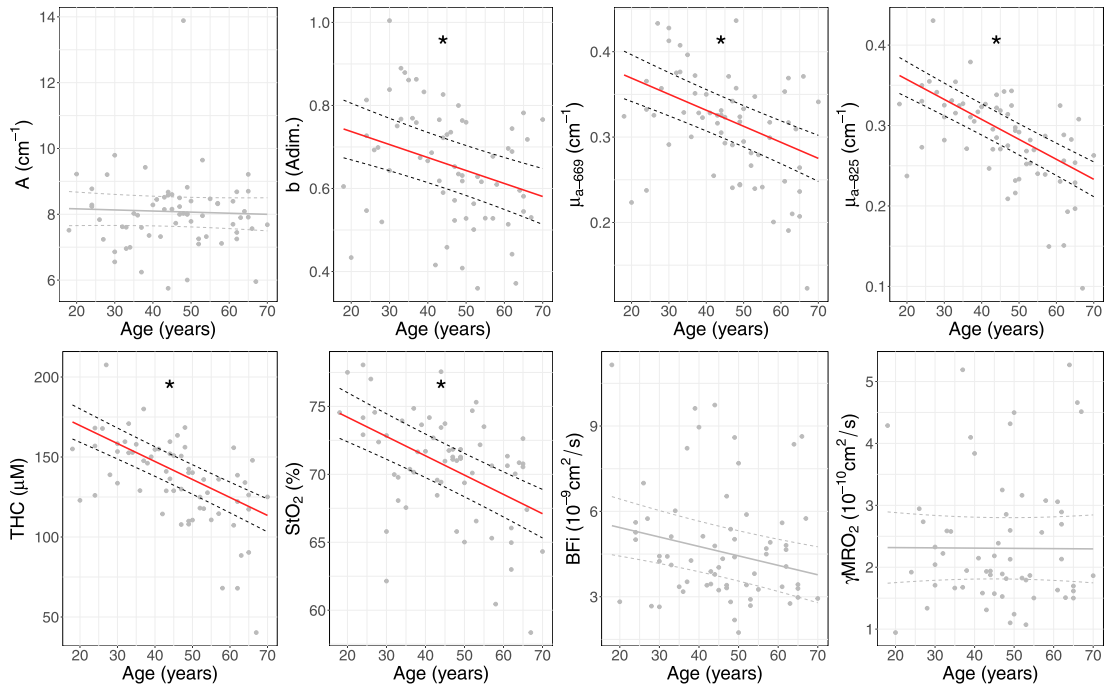

Figure 6. Effect of the subject age on the measured parameters. One data point per each subject, result of the average over repetitions and locations, is reported, together with the statistical model fitted lines. When the correlation is statistically significant, the fitted line are reported in red and highlighted with an asterisk.

3.5. Effect of the presence of thyroid nodules

As the last part, we have investigated whether the presence of a thyroid nodule on the subject's thyroid affects the measured parameters on the sternocleidomastoid muscle, for the long SDS. With this aim, we first have analyzed possible differences between the group of healthy controls and thyroid nodule subjects. The plots highlighting the statistically significant differences between these two groups are reported in figure 9, and results of statistical tests are detailed in table B8.

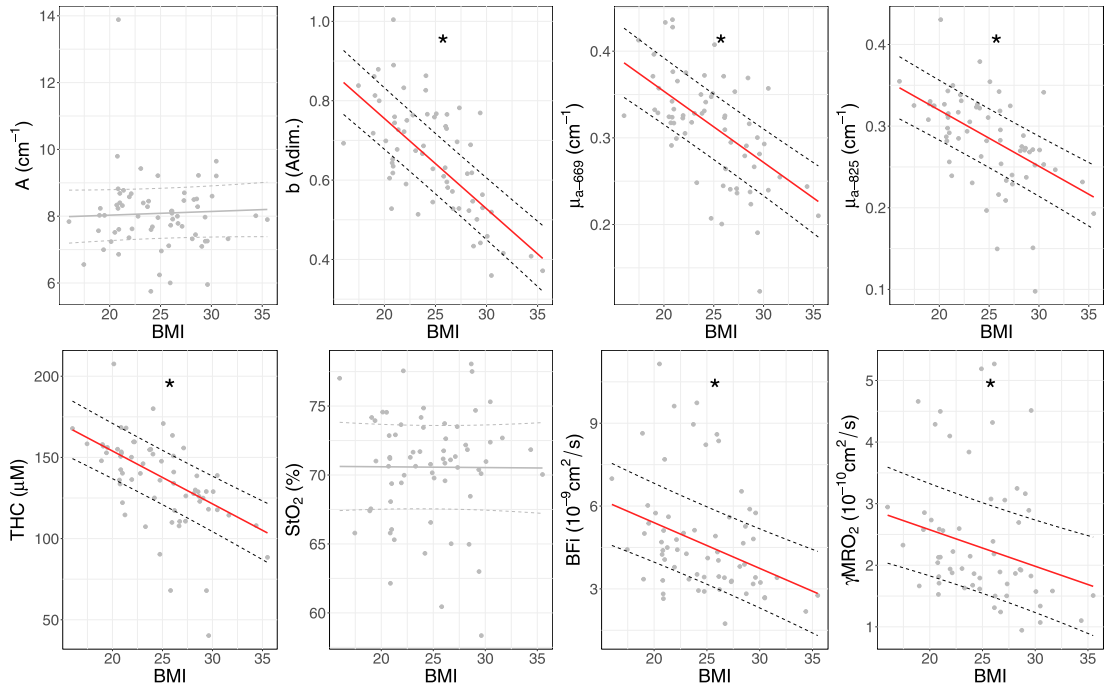

Figure 7. Effect of the subject body mass index BMI on the measured parameters. One data point per each subject, result of the average over repetitions and locations, is reported, together with the statistical model fitted lines. When the correlation is statistically significant, the fitted line are reported in red and highlighted with an asterisk.

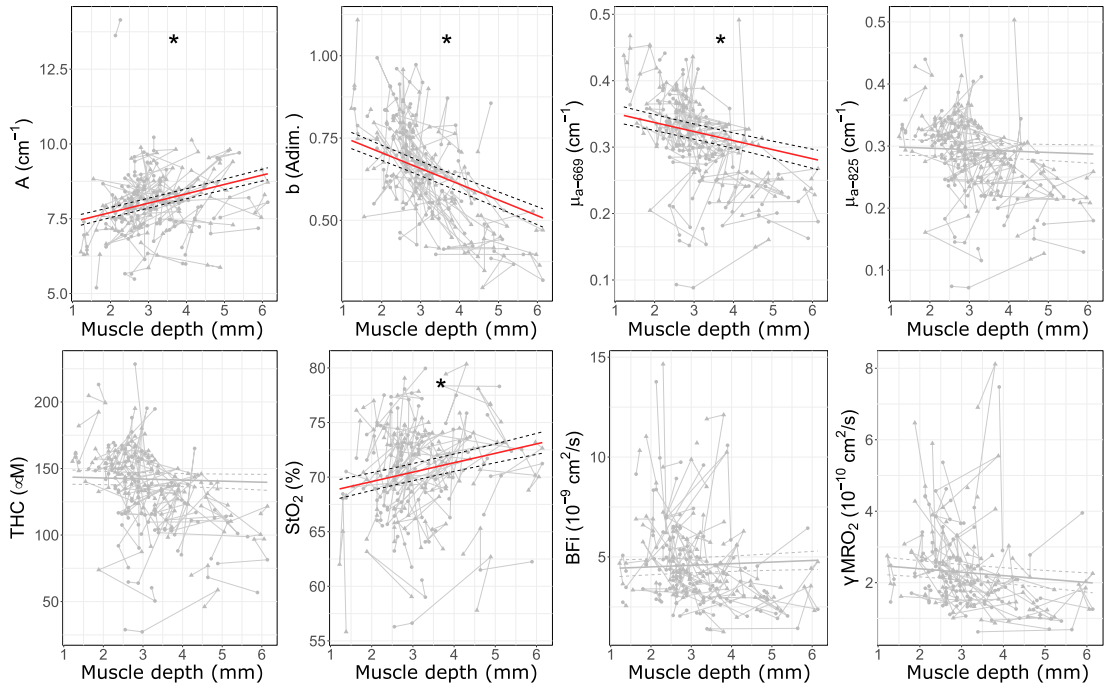

Figure 8. Effect of muscle depth on the measured parameters. One point per repetition (two repetitions and two sides per patient) is reported. Points related to the left side are shown as circles, while to the right side as triangles. Points corresponding to the same subject are connected with gray lines. Data points are reported together with the statistical model fitted lines. When the correlation is statistically significant, the fitted lines are reported in red and highlighted with an asterisk.

Second, we have studied the differences within the group of thyroid nodule subjects, looking at the possible differences between the parameters measured on the muscle at the same side of the neck as the nodule (nodule side), and what measured on the muscle at the opposite side (nodule-free side). The plots are reported in figure 10, and the detailed results of the statistical analysis are reported in table B9, in appendix B.

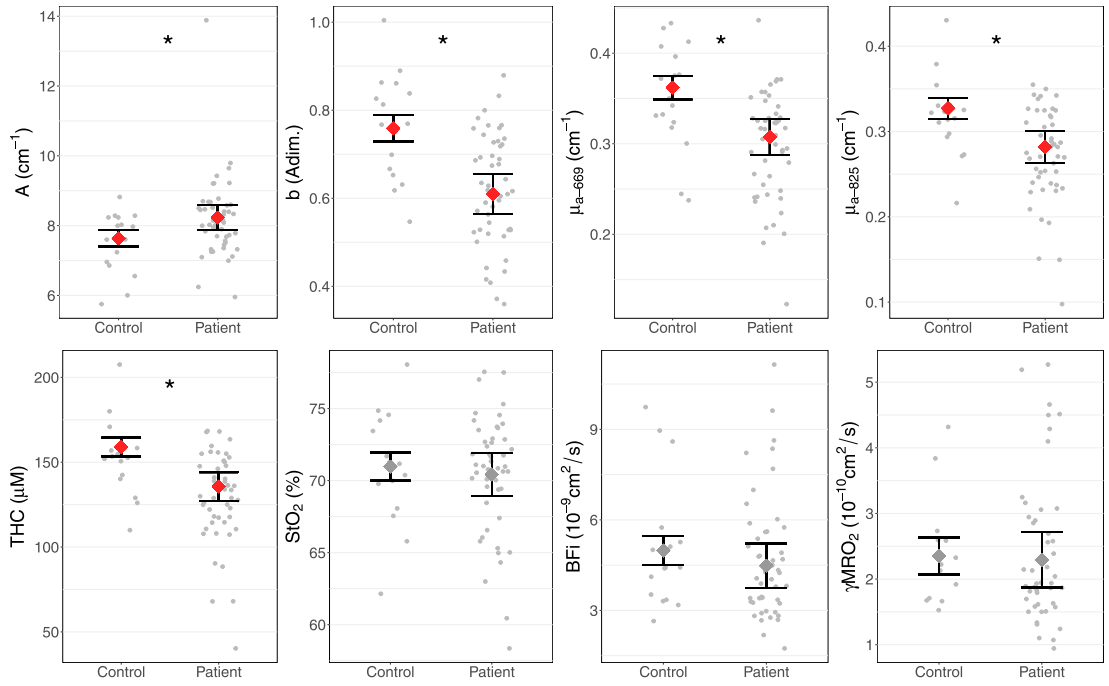

Figure 9. Differences between healthy control and thyroid nodule patient groups. One data point per each subject, result of the average over repetitions and locations, is reported. Model best estimates with error bars are overlapped to data points, and are reported in red and highlighted with an asterisk when differences between groups are statistically significant.

4. Discussion

Our study represents the first characterization of the sternocleidomastoid muscle performed using a multi-modal device simultaneously combining TD-NIRS, DCS and is guided by US imaging (Cortese *et al* 2021a). The results reported in section 3 and discussed here represent a comprehensive reference for future studies utilizing near-infrared diffuse optical methods to measure the SCM hemodynamics and oxygen metabolism. By utilizing a state-of-the-art system with concurrent ultrasound guidance and a large number of wavelengths, we have provided not only parameters for designing new system but also for avoiding confounding effects such as the demographic variables and common pathologies such as the presence of thyroid nodules (Haugen *et al* 2016, Bray *et al* 2018). Figures 2 and 3 and tables in appendix A report the measured physiological and optical parameters. Apart from the preliminary characterization on a small group of subjects performed using a hybrid TD-NIRS/DCS system (Lindner *et al* 2016), the only SCM diffuse optical characterizations reported up to now have been performed by using FD-NIRS or CW-NIRS (Katayama *et al* 2015, Yang *et al* 2020a, Istfan *et al* 2021, Van Hollebeke *et al* 2022), which have shown to be less reliable in measuring absolute values. Most studies report trends in blood oxygenation instead. Albeit the values retrieved in this study show important differences from the literature. For example, respect to the recent study of Istfan *et al* (2021) performed with a FD-NIRS device, we report a systematic overestimation of approximately 10%–30% for variables as scattering coefficient, DPF, and StO_2, and a similar underestimation for absorption coefficient, THC, HbO_2 and Hb.

We explain these trends by considering that the main differences arise from the different technologies and data analysis models used to characterize the muscle. Several studies indeed have highlighted systematic differences between optical measurements obtained with different technologies and, within the same technology, with different devices and/or different analysis methods (Hyttel-Sorensen *et al* 2011, Kleiser *et al* 2016, 2018, Istfan *et al* 2021, Lanka *et al* 2022).

Demographic differences between the two studies can also explain such trends. Istfan *et al* 2021 have considered a reduced group of ten healthy subjects, much younger than the whole population considered in our study. When we limit our analysis only to the younger group of subjects without thyroid nodules (see table B8), these systematic differences tend to be smaller.

Lastly, slightly different position of the probe over the sternocleidomastoid muscle and different body orientation of the subject, can also explain the differences reported in the measured values. Respect to the study of Istfan *et al* (2021), we have indeed considered a less lateral position over the SCM, just at the side of the thyroid lobe, and the subject laying supine instead of seated in upright position as in the study of Istfan *et al* (2021).

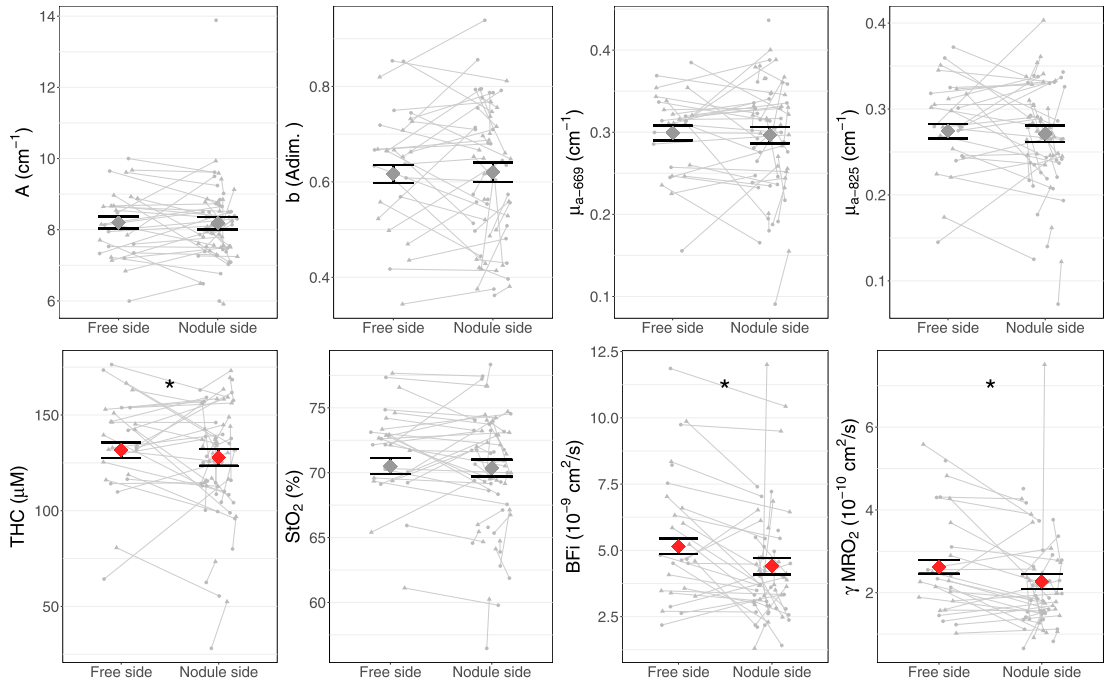

Figure 10. Differences between muscles at the nodule side of the neck and at the 'nodule-free' side, within the group of thyroid nodule patients. One data point per side per each subject, result of the average over repetitions, is reported. Data points corresponding to the left side are represented with circles, and to the right side with triangles. Points correspondent to the same subject are connected by a gray line. Model best estimates with error bars are overlapped to data points, and are reported in red and highlighted with an asterisk when differences between groups are statistically significant.

Figures 2 and 3 and the statistical results reported in sections 3.2 and appendix B highlight differences in the measured parameters due to the source-detector separation used for the measurements as expected since the muscle has significant overlaying tissue.

As well known by light transport theory (Martelli 2009), longer SDS acquisitions are in first approximation more sensitive to photons probing deeper tissue. Shorter source-detector acquisitions, on the other hand, results more affected by photons probing the superficial tissue (in this case skin and fat layer covering the sternocleidomastoid muscle), showing different optical and hemodynamic properties respect to the deeper tissue (Nasseri *et al* 2016, Istfan *et al* 2021, Pirovano *et al* 2021).

The recorded differences between long and short SDS results (table B1) are remarkable for perfusion and scattering related parameters (~10%−20%) and smaller for absorption related parameters, such as hemoglobin content and saturation (<4%).

We explain such small differences by considering that short SDS channel can be sensitive to muscle properties too, since the average muscle depth is 3.1 mm and the long and short SDS channels only differ of 6 mm (long SDS: 2.5 cm, short SDS: 1.9 cm) (Istfan *et al* 2021). In this respect, future studies with the aim of improve the depth sensitivity applying multi-distance detection and layered analytical/numerical models, should consider a smaller source-detector separation for the short SDS channel, in order to better take care of the superficial tissue properties.

A well-known challenge of diffuse optical NIRS technologies is the limited spatial resolution, that can lead to large variability in the measured parameters. We have tried to address this point by analyzing the precision of our measurements in details. The data reported in table A3, comparing the precision of single and multiple acquisitions to the group variability, underline the high quality of the measurements performed. Such precision result in line with the laboratory characterization of the device used (Cortese *et al* 2021a), and well allow the detection of physiological changes due to SCM and other muscle activation due to exercise training or pathological situation (Yu *et al* 2005, Guenette *et al* 2011, Shadgan *et al* 2011, Gurley *et al* 2012, Shang *et al* 2013, Katayama *et al* 2015, Basoudan *et al* 2016, Reid *et al* 2016, Perrey and Ferrari 2018, Tanaka *et al* 2018, Quaresima *et al* 2019, Rodrigues *et al* 2020, Giovannella *et al* 2021, Istfan *et al* 2021).

In particular, we do not reveal differences between precision of short SDS and long SDS acquisitions, the last characterized by a much lower detection count-rate (data not shown). This point demonstrates that the main contribution to the variability of a single acquisition comes from physiological changes during the acquisition

time (∼100 s). This is promising in light of the possibility of drastically reducing the measurement integration time to improve the device temporal resolution without affecting the precision (Cortese *et al* 2021b).

The variability over probe repositioning on the same location, is both affected by physiological changes in the tissue between the two different repetitions, and by errors in finding the exact same position of the probe in the neck. This point is also strengthened by the differences measured in muscle depth and thickness between the first and second repetition on the same location, CV rep. ∼ 9 %. In this respect, the proposed multi-modal approach combining optical measurements guided by simultaneous US imaging helps to reduce the impact of probe position errors in the measurement precision.

With regard to the differences between muscle location, reported in figure 4 and table B2, we note that all the optical and hemodynamic variables show significant differences. Small hemodynamic differences between sides of the neck have already been observed (Lindner *et al* 2016, Lindner 2017). In these references, Lindner *et al* explained such differences with muscle activation due to neck hyperextended position, inducing hemodynamics changes during the measurement protocol. In that case, for all the subjects, the first location to be measured was the right side, and last the left side. In the present study, we also have noted statistical differences between the first side of the neck measured in each patient and the second side (significant differences in A, b, BFi and γMRO_2—data not shown). However, due to randomization of the starting measurement side (see section 2.2), this does not effect the previous results comparing left and right sides as a group.

Figure 5 and table B3 highlight differences on the measured parameters between sexes. The contrast of hemodynamic and optical variables between sexes have been also noticed previously (Farzam *et al* 2014, Istfan *et al* 2021). Such variations can be linked to *BMI* differences between the two groups, since, as reported in table 1, they are statistically significant. As reported in section 3.4 and discussed later on, it is indeed well known that BMI affects NIRS acquisitions (Durduran *et al* 2002, Spinelli *et al* 2004, Pirovano *et al* 2021). Additionally, different muscle mass (i.e. thickness) between sexes (see table 1) may be responsible of the differences detected between the two groups. Lastly, such variations can be explained by different hemoglobin content between sexes (Murphy 2014), also detected with blood analysis test among the population of this study (data not presented).

In figures 6, 7 and 8 we have reported the correlations between the measured parameters and age, BMI and muscle depth respectively. These three parameters are linearly positively correlated (see table B10): BMI and muscle depth are a measure of the presence of a thicker fat superficial layer, which is prominent in older population. As BMI and muscle depth increase, our measurement will be indeed more sensitive to the thicker superficial layer of adipose tissue, which has a different hemodynamics and composition than muscle (Nasseri *et al* 2016, Istfan *et al* 2021, Pirovano *et al* 2021).

Considering the muscle depth dependence of the optically measured parameters is of key importance, due to its large variability (>30%) between subjects, as reported in table A3. By the means of the multi-modal optical-US device used, and by the statistical analysis reported, we aim to reduce the effect of such variability in the optically derived parameters, setting the path for being more sensitive to the specific tissue under investigation. The simultaneous acquisition of US images indeed allows to re-normalize the optical parameters by taking into account the muscle depth as reported in section 3. In the future, the anatomical information carried by US, should come together with advanced computational analysis methods, such as Monte Carlo and finite element methods (Fang 2010, Jermyn *et al* 2013), capable of modelling light propagation using segmented US images. Such methods should be furthermore integrated with novel systems allowing multiple source detector distance acquisitions for a better separation between superficial and deep tissue properties (Wang *et al* 2022).

In addition, we would like to make a last comment on the dependence of the measured parameters on muscle depth, reported in figure 8. We note that, we have acquired one US depth measurement for every repetition and location (so, four depth values measured per subject, two repetitions per side). The average variability between repetitions is ∼9 %, as reported in table A3. This variability can in principle hide the dependencies of the measured hemodynamic parameters on the thickness of the fat layer tissue. Differences on measured depth among repetitions on the same subject could indeed reflect differences of probe pressure on subject neck more than anatomical differences (i.e. thicker fat layer), that can significantly impact on the local hemodynamics (Mesquita *et al* 2013, Farzam *et al* 2014, Baker *et al* 2015).

With regard to the differences between healthy control and thyroid patient groups reported in section 3.5, they possibly mainly reflect the age, BMI and muscle depth differences between the two groups. Healthy subjects are indeed in average younger, and with lower BMI and muscle depth than patients (table 1). Lastly, the slight differences reported among the patient group between the nodule side and nodule-free side of the neck, could supposedly reflect small anatomical differences between the two neck regions, with and without nodule.

As last point, we would like to comment on the clinical relevance of the present study. Our work, together with the previously-mentioned studies (Guenette *et al* 2011, Shadgan *et al* 2011, Katayama *et al* 2015, Basoudan *et al* 2016, Reid *et al* 2016, Tanaka *et al* 2018, Rodrigues *et al* 2020, Istfan *et al* 2021, Gømez *et al* 2023) using different near-infrared diffuse optical devices, have shown that diffuse optical technologies are among the new technologies capable of non-invasively monitoring the SCM activity. Additionally to NIRS studies, we also

mention here promising results of photoacoustic imaging in monitoring skeletal muscle activity (Yang *et al* 2020b, Karlas *et al* 2020, Wagner *et al* 2021). In this respect, albeit photoacoustic imaging spatial resolution is better than diffuse optical technology resolution, such technology is unable to provide a direct measure of blood perfusion, which is made available by the device used in this study.

Monitoring the activity of the SCM muscle can be of great importance in cases of patients with severe respiratory distress such as COPD. Since the SCM muscle acts as an accessory respiratory muscle, it is indeed recruited to aid in respiration in such cases, when primary respiratory muscle effort, such as diaphragm, is not sufficient. By monitoring SCM activity, information can be obtained on the degree of the patient's respiratory effort that is required to maintain an optimal minute ventilation (Guenette *et al* 2011, Shadgan *et al* 2011, Katayama *et al* 2015, Basoudan *et al* 2016, Reid *et al* 2016, Tanaka *et al* 2018, Rodrigues *et al* 2020).

In particular, SCM monitoring would be relevant in more acute settings in the intensive care unit (ICU), such as acute respiratory failure, in order to establish the necessity of mechanical respiratory support, or to decide whether the ventilator support is no longer needed. On that behalf, SCM monitoring may be of special interest to determine the readiness of an intubated patient for weaning from ventilation (Reid *et al* 2016, Istfan *et al* 2021). In this context, only few physiological parameters have demonstrated predictive power, and new tools for improving weaning success are urgently needed (Meade *et al* 2001, Funk *et al* 2010). When failure from weaning from ventilation occurs, the cardiovascular system is unable to meet the increased oxygen cost of breathing (Field *et al* 1982, Vassilakopoulos *et al* 1996). Usually, the increased oxygen cost of breathing during extubation and/or spontaneous breathing trial (SBT) process, is met by redirecting blood flow from the periphery towards the primary respiratory muscles, such as the diaphragm, and accessory respiratory muscles as the SCM (Gruartmoner *et al* 2014, Mesquida *et al* 2020). Anyway, long ICU stay and prolonged invasive mechanical ventilation, can cause dysfunction and atrophy to respiratory muscles, which, during the extubation or SBT phase, are not able to cope with the increased oxygen cost of breathing. In this respect, no activation or, on the other hand, early and elevated activation of the SCM during the SBT have been associated to weaning failures, reflecting the inability of primary respiratory muscles to resume autonomous respiration (Parthasarathy *et al* 2007, Dres *et al* 2017, Dres and Demoule 2018, Dres *et al* 2020, Van Hollebeke *et al* 2022).

In such framework, non-invasive monitoring of SCM hemodynamics through near-infrared spectroscopies before and during the spontaneous breathing trial and within the early extubation phases, may add important additional biomarkers for determining the right moment for extubation, drastically reducing the failure rate, or for early detecting extubation failure and the need for rapid re-institution of mechanical ventilation (Reid *et al* 2016, Istfan *et al* 2021).

5. Conclusion

In this paper we have reported a detailed *in vivo* optical and hemodynamic characterization of the human sternocleidomastoid muscle. The characterization has been performed by using a state-of-the-art multi-modal optical-ultrasound integrated device, combining in a single system a clinical ultrasound, and two cutting edge diffuse optical systems, TD-NIRS and DCS, capable of simultaneously providing hemodynamic and anatomical information of the tissue.

Here, we have reported detailed plots and tables, related to the sternocleidomastoid muscle of sixty-five subjects including healthy population and thyroid nodule patients, with the average values and variabilities of hemodynamic and optical parameters. In addition, we have evaluated, by a rigorous statistical analysis, the dependencies of all the measured parameters on the location of the muscle (left or right side of the neck), on sex, on age, body mass index and depth of the muscle (obtained through simultaneous US acquisitions). Lastly, we have evaluated whether the measured muscle hemodynamics is affected by the presence of a thyroid nodule on the same side of the neck, being this situation very common among the adult population.

Concluding, we posit that the unique platform together with the rigorous analysis reported allows these results to pave the way for future near-infrared spectroscopic studies and clinical applications on SCM hemodynamic monitoring. Lastly, the systematic analysis of the correlations between the retrieved hemodynamic and optical parameters and variables such as side of the neck, sex, age, body mass index and depth of the muscle, will allow future studies to take into account such dependencies.

Acknowledgments

This work has received funding from: the European Union's Horizon 2020 research and innovation programme under grant agreements No. 688303 (LUCA), No. 101016087 (VASCOVID), No. 101017113 (TINYBRAINS), No. 675332 (BITMAP), No. 871124 (LASERLAB-EUROPE V), Fundació CELLEX Barcelona, Fundació Mir-Puig, Agencia Estatal de Investigación (PHOTOMETABO, PID2019-106481RB-C31/10.13039/

501100011033), the 'Severo Ochoa' Programme for Centres of Excellence in R&D (CEX2019-000910-S), LUX4MED special program, the Obra social 'la Caixa' Foundation (LlumMedBcn), Generalitat de Catalunya (CERCA, AGAUR-2022-SGR-01457, RIS3CAT-001-P-001682 CECH). Additionally, this project has received funding from the Secretaria d'Universitats i Recerca del Departament d'Empresa i Coneixement de la Generalitat de Catalunya, as well as the European Social Fund (L'FSE inverteix en el teu futur)FEDER. The author's have confirmed that any identifiable participants in this study have given their consent for publication. Finally, we sincerely thank the subjects involved in this study for their enthusiastic participation.

Data availability statement

The data that support the findings of this study are openly available at the following URL/DOI:https://doi.org/10.5281/zenodo.7741369 (Cortese *et al* 2023).

Disclosure

The role in the project of all the companies (HemoPhotonics S.L., Vermon SA, IMV Imaging) and their employees involved has been defined by the project objectives, tasks, and work packages and has been reviewed by the European Commission (European Union's Horizon 2020 research and innovation programme, LUCA project, grant agreement No. 688303).

ICFO has equity ownership in the spin-off company HemoPhotonics S.L. and UMW is the CEO. TD and UMW are inventors on relevant patents.

MB, DC, ADM, AT are co-founders of PIONIRS s.r.l., spin off company from Politecnico di Milano (Italy), and MB is the CEO of the company. Their involvement in the study was mainly prior to the company foundation.

All the potential financial conflicts of interest and objectivity of research have been monitored by ICFO's Knowledge and Technology Transfer Department.

Appendix A. Tables of optical and physiological parameters

Table A1. Table of the optically derived physiological parameters (mean ± standard error of the mean) for long and short SDSs. Long SDS: 2.5 cm; short SDS: 1.9 cm.

Sex	SDS	StO_2 (%)	THC (μM)	HbO_2 (μM)	Hb (μM)	BFi (10^{-9} cm^2 s^{-1})	γMRO_2 (10^{-10} cm^2 s^{-1})
All	Long	70.6 ± 0.4	135 ± 3	96 ± 2	39.1 ± 0.7	4.8 ± 0.2	2.4 ± 0.1
Male	Long	71.2 ± 0.7	138 ± 7	99 ± 5	38.7 ± 1.8	5.4 ± 0.5	2.9 ± 0.3
Female	Long	70.4 ± 0.4	134 ± 3	95 ± 2	39.3 ± 0.8	4.6 ± 0.2	2.2 ± 0.1
All	Short	72.1 ± 0.4	139 ± 3	100 ± 2	38.1 ± 0.7	4.0 ± 0.2	1.9 ± 0.1
Male	Short	71.4 ± 0.8	140 ± 8	101 ± 6	38.9 ± 1.9	4.6 ± 0.3	2.6 ± 0.3
Female	Short	72.3 ± 0.4	138 ± 3	100 ± 2	37.9 ± 0.8	3.8 ± 0.2	1.7 ± 0.1

Table A2. Table of the retrieved Mie scattering coefficients A and b (mean ± standard error of the mean), from the relation $\mu_s'(\lambda) = A \cdot (\lambda/\lambda_0)^{-b}$.

Sex	SDS	λ_0 (nm)	A (cm^{-1})	b (adim.)
All	Long	785	8.0 ± 0.1	0.66 ± 0.01
Male	Long	785	7.2 ± 0.2	0.68 ± 0.02
Female	Long	785	8.2 ± 0.1	0.65 ± 0.02
All	Short	785	9.6 ± 0.2	0.70 ± 0.02
Male	Short	785	8.4 ± 0.2	0.76 ± 0.03
Female	Short	785	9.9 ± 0.2	0.69 ± 0.02

Table A3. Table of the variability of the principal physiological and optical parameters for long and short SDSs. Variability due to single acquisition (CV single) fluctuations, due to probe repositioning between two repetitions on the same location (CV rep.) and variability within the whole study population (CV group) are reported.

	SDS	Depth	Thickness	A	b	μ_{a-669}	μ_{a-825}	THC	StO_2	BFi	γMRO_2
CV single	Long	–	–	0.4%	3.0%	2.0%	1.2%	1.0%	0.9%	5.3%	6.0%
CV rep.	Long	8.5%	8.7%	4.1%	7.1%	6.5%	6.6%	6.8%	2.2%	13.0%	15.0%
CV group	Long	32.2%	22.8%	13.2%	22.3%	21.4%	19.6%	21.7%	6.0%	46.1%	47.6%
CV single	Short	–	–	0.4%	3.1%	2.5%	1.5%	0.8 %	0.8%	5.5%	5.9%
CV rep.	Short	8.5%	8.7%	4.7%	7.3%	6.2%	6.2%	6.0 %	2.0%	12.2%	14.3%
CV group	Short	32.2%	22.8%	21.7%	27.4%	21.3%	20.5%	21.6%	5.6%	47.5%	45.5%

Table A4. Table of the measured reduced scattering coefficients μ_s' (mean ± standard error of the mean).

Sex	SDS	μ_{s-637}' (cm^{-1})	μ_{s-669}' (cm^{-1})	μ_{s-722}' (cm^{-1})	μ_{s-825}' (cm^{-1})	μ_{s-841}' (cm^{-1})	μ_{s-905}' (cm^{-1})	μ_{s-971}' (cm^{-1})	μ_{s-1050}' (cm^{-1})
All	Long	9.1 ± 0.1	8.9 ± 0.1	8.4 ± 0.1	7.7 ± 0.1	7.6 ± 0.1	7.3 ± 0.1	7.0 ± 0.1	6.6 ± 0.1
Male	Long	8.2 ± 0.2	7.9 ± 0.2	7.6 ± 0.2	6.9 ± 0.2	6.8 ± 0.2	6.5 ± 0.1	6.2 ± 0.1	5.9 ± 0.1
Female	Long	9.5 ± 0.1	9.2 ± 0.1	8.7 ± 0.1	8.0 ± 0.1	7.9 ± 0.1	7.6 ± 0.1	7.2 ± 0.1	6.9 ± 0.1
All	Short	10.8 ± 0.2	10.5 ± 0.2	9.9 ± 0.2	9.0 ± 0.2	8.9 ± 0.2	8.5 ± 0.2	8.1 ± 0.2	7.7 ± 0.2
Male	Short	9.5 ± 0.2	9.2 ± 0.2	8.7 ± 0.2	7.9 ± 0.2	7.8 ± 0.2	7.3 ± 0.2	7.0 ± 0.2	6.6 ± 0.2
Female	Short	11.3 ± 0.2	10.9 ± 0.2	10.3 ± 0.2	9.5 ± 0.2	9.3 ± 0.2	8.9 ± 0.2	8.5 ± 0.2	8.1 ± 0.2

Table A5. Table of the measured absorption coefficients μ_a (mean $\pm$ standard error of the mean).

Sex	SDS	μ_{a-637} (cm^{-1})	μ_{a-669} (cm^{-1})	μ_{a-722} (cm^{-1})	μ_{a-825} (cm^{-1})	μ_{a-841} (cm^{-1})	μ_{a-905} (cm^{-1})	μ_{a-971} (cm^{-1})	μ_{a-1050} (cm^{-1})
All	Long	0.39 ± 0.01	0.31 ± 0.01	0.24 ± 0.01	0.29 ± 0.01	0.30 ± 0.01	0.38 ± 0.01	0.56 ± 0.01	0.37 ± 0.01
Male	Long	0.40 ± 0.02	0.31 ± 0.01	0.25 ± 0.01	0.29 ± 0.01	0.31 ± 0.01	0.39 ± 0.02	0.58 ± 0.02	0.37 ± 0.01
Female	Long	0.39 ± 0.01	0.31 ± 0.01	0.24 ± 0.01	0.28 ± 0.01	0.30 ± 0.01	0.38 ± 0.01	0.55 ± 0.01	0.37 ± 0.01
All	Short	0.39 ± 0.01	0.32 ± 0.01	0.25 ± 0.01	0.30 ± 0.01	0.31 ± 0.01	0.38 ± 0.01	0.57 ± 0.01	0.37 ± 0.01
Male	Short	0.41 ± 0.02	0.32 ± 0.01	0.25 ± 0.01	0.30 ± 0.01	0.32 ± 0.01	0.40 ± 0.02	0.60 ± 0.02	0.38 ± 0.02
Female	Short	0.39 ± 0.01	0.32 ± 0.01	0.25 ± 0.01	0.29 ± 0.01	0.31 ± 0.01	0.38 ± 0.01	0.56 ± 0.01	0.37 ± 0.01

Table A6. Table of the measured differential pathlength factors DPF (mean ± standard error of the mean).

Sex	SDS	DPF_{637} (*adim.*)	DPF_{669} (*adim.*)	DPF_{722} (*adim.*)	DPF_{825} (*adim.*)	DPF_{841} (*adim.*)	DPF_{905} (*adim.*)	DPF_{971} (*adim.*)	DPF_{1050} (*adim.*)
All	Long	3.82 ± 0.04	4.20 ± 0.04	4.72 ± 0.06	4.32 ± 0.04	4.21 ± 0.05	3.80 ± 0.04	3.16 ± 0.04	4.08 ± 0.05
Male	Long	3.61 ± 0.09	4.00 ± 0.10	4.44 ± 0.12	4.12 ± 0.12	4.01 ± 0.12	3.61 ± 0.09	2.99 ± 0.10	3.93 ± 0.12
Female	Long	3.90 ± 0.04	4.26 ± 0.04	4.81 ± 0.07	4.38 ± 0.05	4.28 ± 0.05	3.87 ± 0.04	3.21 ± 0.04	4.13 ± 0.05
All	Short	4.05 ± 0.05	4.38 ± 0.05	4.87 ± 0.05	4.39 ± 0.05	4.32 ± 0.05	3.90 ± 0.04	3.24 ± 0.04	4.10 ± 0.05
Male	Short	3.75 ± 0.09	4.10 ± 0.09	4.52 ± 0.10	4.13 ± 0.11	4.05 ± 0.10	3.64 ± 0.09	3.00 ± 0.08	3.90 ± 0.10
Female	Short	4.16 ± 0.05	4.48 ± 0.06	4.98 ± 0.06	4.48 ± 0.05	4.41 ± 0.05	3.99 ± 0.05	3.32 ± 0.05	4.17 ± 0.05

Appendix B. Tables of statistical tests

Table B1. Table of LME estimates, standard errors and statistical tests. Source-detector separation differences.

	Long SDS	Short SDS	Absolute difference	Relative difference (%)	$p-$value
$A\,(\mathrm{cm}^{-1})$	8.1 ± 0.1	9.5 ± 0.1	1.46 ± 0.04	16.6 ± 0.5	$<10^{-3}$
$b(adim.)$	0.65 ± 0.02	0.72 ± 0.02	0.070 ± 0.004	10.2 ± 0.6	$<10^{-3}$
$\mu_{a-669}\,(\mathrm{cm}^{-1})$	0.321 ± 0.007	0.324 ± 0.007	0.003 ± 0.002	0.8 ± 0.6	0.12
$\mu_{a-825}\,(\mathrm{cm}^{-1})$	0.295 ± 0.007	0.307 ± 0.007	0.011 ± 0.002	3.8 ± 0.7	$<10^{-3}$
THC $(\mu\mathrm{M})$	141 ± 3	145 ± 3	4.2 ± 0.4	2.9 ± 0.3	$<10^{-3}$
$StO_2(\%)$	70.6 ± 0.5	71.7 ± 0.5	1.07 ± 0.07	1.5 ± 0.1	$<10^{-3}$
BFi $(10^{-9}\ \mathrm{cm}^2\ \mathrm{s}^{-1})$	4.7 ± 0.2	4.0 ± 0.2	0.71 ± 0.03	16.3 ± 0.8	$<10^{-3}$
$\gamma MRO_2\,(10^{-10}\ \mathrm{cm}^2\ \mathrm{s}^{-1})$	2.3 ± 0.1	1.9 ± 0.1	0.40 ± 0.03	19 ± 1	$<10^{-3}$

Table B2. Table of LME estimates, standard errors and statistical tests. Location differences.

	Left	Right	Absolute difference	Relative difference (%)	$p-$value
$A\,(\mathrm{cm}^{-1})$	7.9 ± 0.1	8.1 ± 0.1	0.20 ± 0.03	2.5 ± 0.4	$<10^{-3}$
$b(adim.)$	0.67 ± 0.02	0.64 ± 0.02	0.033 ± 0.005	5.1 ± 0.7	$<10^{-3}$
$\mu_{a-669}\,(\mathrm{cm}^{-1})$	0.301 ± 0.008	0.323 ± 0.008	0.022 ± 0.003	7.0 ± 0.9	$<10^{-3}$
$\mu_{a-825}\,(\mathrm{cm}^{-1})$	0.274 ± 0.007	0.295 ± 0.008	0.021 ± 0.003	7 ± 1	$<10^{-3}$
THC $(\mu\mathrm{M})$	130 ± 3	140 ± 4	10 ± 1	7.5 ± 0.7	$<10^{-3}$
$StO_2\,(\%)$	70.4 ± 0.5	70.8 ± 0.5	0.4 ± 0.2	0.6 ± 0.3	0.01
BFi $(10^{-9}\ \mathrm{cm}^2\ \mathrm{s}^{-1})$	4.4 ± 0.2	5.1 ± 0.3	0.63 ± 0.07	13 ± 1	$<10^{-3}$
$\gamma MRO_2\,(10^{-10}\ \mathrm{cm}^2\ \mathrm{s}^{-1})$	2.2 ± 0.1	2.5 ± 0.1	0.27 ± 0.05	12 ± 2	$<10^{-3}$

Table B3. Table of LME estimates, standard errors and statistical tests. Sex differences.

	Female	Male	Absolute difference	Relative difference (%)	$p-$value
$A\,(\mathrm{cm}^{-1})$	8.3 ± 0.1	7.4 ± 0.3	0.9 ± 0.3	12 ± 3	$<10^{-3}$
$b(adim.)$	0.65 ± 0.02	0.67 ± 0.04	0.03 ± 0.04	4 ± 6	0.51
$\mu_{a-669}\,(\mathrm{cm}^{-1})$	0.319 ± 0.008	0.33 ± 0.02	0.01 ± 0.02	4 ± 6	0.40
$\mu_{a-825}\,(\mathrm{cm}^{-1})$	0.291 ± 0.008	0.31 ± 0.02	0.02 ± 0.02	6 ± 6	0.28
THC $(\mu\mathrm{M})$	140 ± 4	151 ± 8	11 ± 7	8 ± 5	0.13
$StO_2(\%)$	70.4 ± 0.6	71 ± 1	0.8 ± 1	1 ± 1	0.48
BFi $(10^{-9}\ \mathrm{cm}^2\ \mathrm{s}^{-})$	4.5 ± 0.3	5.2 ± 0.6	0.7 ± 0.6	20 ± 10	0.20
$\gamma MRO_2\,(10^{-10}\ \mathrm{cm}^2\ \mathrm{s}^{-1})$	2.2 ± 0.1	2.9 ± 0.3	0.7 ± 0.3	30 ± 10	0.02

Table B4. Table of LME estimates, standard errors and statistical tests. Age dependence.

	Intercept	Slope (unit/year)	$p-$value
$A\,(\mathrm{cm}^{-1})$	8.2 ± 0.4	-0.003 ± 0.009	0.72
$b(adim.)$	0.80 ± 0.06	-0.003 ± 0.001	0.01
$\mu_{a-669}\,(\mathrm{cm}^{-1})$	0.41 ± 0.02	-0.0019 ± 0.0005	$<10^{-3}$
$\mu_{a-825}\,(\mathrm{cm}^{-1})$	0.41 ± 0.02	-0.0025 ± 0.0004	$<10^{-3}$
THC $(\mu\mathrm{M})$	192 ± 9	-1.1 ± 0.2	$<10^{-3}$
$StO_2(\%)$	77 ± 2	-0.14 ± 0.03	$<10^{-3}$
BFi $(10^{-9}\ \mathrm{cm}^2\ \mathrm{s}^{-1})$	6.1 ± 0.9	-0.03 ± 0.02	0.08
$\gamma MRO_2\,(10^{-10}\ \mathrm{cm}^2\ \mathrm{s}^{-1})$	2.3 ± 0.5	-0.0004 ± 0.01	0.97

Table B5. Table of LME estimates, standard errors and statistical tests. BMI dependence. We also report the logarithm of μ_{a-669}, μ_{a-825}, BFi and γMRO_2 as independent variables, since we have found that an exponential model better describe the relation between these variables and BMI.

	Intercept	Slope (unit/(kg m^{-2}))	$p-$value
A (cm^{-1})	7.8 ± 0.7	0.01 ± 0.03	0.71
b(*adim.*)	1.21 ± 0.08	-0.023 ± 0.003	$<10^{-3}$
μ_{a-669} (cm^{-1})	0.52 ± 0.04	-0.008 ± 0.002	$<10^{-3}$
μ_{a-825} (cm^{-1})	0.46 ± 0.04	-0.007 ± 0.001	$<10^{-3}$
THC (μM)	220 ± 20	-3.3 ± 0.7	$<10^{-3}$
StO_2 (%)	71 ± 3	-0.006 ± 0.1	0.96
BFi (10^{-9} cm^2 s^{-1})	9 ± 1	-0.17 ± 0.06	0.004
γMRO_2 (10^{-10} cm^2 s^{-1})	3.8 ± 0.7	-0.06 ± 0.03	0.046
$\log(\mu_{a-669}/(\text{cm}^{-1}))$	-0.6 ± 0.1	-0.023 ± 0.005	$<10^{-3}$
$\log(\mu_{a-825}/(\text{cm}^{-1}))$	-0.8 ± 0.1	-0.018 ± 0.006	0.004
$\log(\text{BFi}/(10^{-9}\text{cm}^2\text{s}^{-1}))$	2.4 ± 0.3	-0.04 ± 0.01	$<10^{-3}$
$\log(\gamma MRO_2/(10^{-10}\text{cm}^2\text{s}^{-1}))$	1.6 ± 0.3	-0.03 ± 0.01	0.004

Table B6. Table of LME estimates, standard errors and statistical tests. Muscle depth dependence. We also report the logarithm of γMRO_2 as independent variable, since we have found that an exponential model better describe the relation between this variable and muscle depth.

	Intercept	Slope (unit/mm)	$p-$value
A(cm^{-1})	7.1 ± 0.2	0.31 ± 0.04	$<10^{-3}$
b(*adim.*)	0.80 ± 0.02	-0.048 ± 0.006	$<10^{-3}$
μ_{a-669} (cm^{-1})	0.36 ± 0.01	-0.014 ± 0.003	$<10^{-3}$
μ_{a-825} (cm^{-1})	0.30 ± 0.01	-0.002 ± 0.003	0.48
THC (μM)	144 ± 5	-0.8 ± 1	0.52
StO_2 (%)	67.9 ± 0.8	0.9 ± 0.2	$<10^{-3}$
BFi (10^{-9} cm^2 s^{-1})	4.3 ± 0.4	0.08 ± 0.09	0.39
γMRO_2 (10^{-10} cm^2 s^{-1})	2.6 ± 0.2	-0.10 ± 0.06	0.09
$\log(\gamma MRO_2/(10^{-10}\text{cm}^2\text{s}^{-1}))$	0.97 ± 0.08	-0.07 ± 0.02	$<10^{-3}$

Table B7. Table of LME estimates, standard errors and statistical tests. Muscle thickness dependence.

	Intercept	Slope (unit/mm)	$p-$value
A (cm^{-1})	7.6 ± 0.2	0.08 ± 0.02	$<10^{-3}$
b(*adim.*)	0.74 ± 0.03	-0.012 ± 0.003	$<10^{-3}$
μ_{a-669} (cm^{-1})	0.30 ± 0.01	0.004 ± 0.002	0.02
μ_{a-825} (cm^{-1})	0.25 ± 0.01	0.008 ± 0.001	$<10^{-3}$
THC (μM)	121 ± 5	3.0 ± 0.6	$<10^{-3}$
StO_2 (%)	67.0 ± 0.8	0.54 ± 0.09	$<10^{-3}$
BFi (10^{-9} cm^2 s^{-1})	4.7 ± 0.4	-0.02 ± 0.04	0.69
γMRO_2 (10^{-10} cm^2 s^{-1})	2.9 ± 0.2	-0.09 ± 0.03	0.001

Table B8. Table of LME estimates, standard errors and statistical tests. Patients Vs. healthy subjects.

	Control	Patient	Absolute difference	Relative difference (%)	$p-$value
A (cm^{-1})	7.6 ± 0.2	8.2 ± 0.4	0.6 ± 0.3	7 ± 4	0.03
b(*adim.*)	0.76 ± 0.03	0.61 ± 0.05	0.15 ± 0.03	22 ± 3	$<10^{-3}$
μ_{a-669} (cm^{-1})	0.36 ± 0.01	0.31 ± 0.02	0.05 ± 0.02	16 ± 5	$<10^{-3}$
μ_{a-825} (cm^{-1})	0.33 ± 0.01	0.28 ± 0.02	0.05 ± 0.01	15 ± 3	0.002
THC (μM)	159 ± 6	136 ± 8	23 ± 6	16 ± 3	$<10^{-3}$
StO_2(%)	71 ± 1	70 ± 1	0.5 ± 1	0.8 ± 1	0.63
BFi (10^{-9} cm^2 s^{-1})	5.0 ± 0.5	4.5 ± 0.7	0.5 ± 0.6	10 ± 10	0.36
γMRO_2 (10^{-10} cm^2 s^{-1})	2.4 ± 0.3	2.3 ± 0.4	0.06 ± 0.3	3 ± 10	0.85

Table B9. Table of LME estimates, standard errors and statistical tests. Nodule versus Nodule-free sides (only thyroid nodule patients).

	Nodule-free side	Nodule side	Absolute difference	Relative difference (%)	$p-$value
$A\,(\mathrm{cm}^{-1})$	8.2 ± 0.2	8.2 ± 0.2	0.02 ± 0.05	0.2 ± 0.6	0.76
$b\,(adim.)$	0.62 ± 0.02	0.62 ± 0.02	0.003 ± 0.007	0.5 ± 1	0.67
$\mu_{a-669}\,(\mathrm{cm}^{-1})$	0.299 ± 0.009	0.30 ± 0.01	0.003 ± 0.004	0.9 ± 1	0.53
$\mu_{a-825}\,(\mathrm{cm}^{-1})$	0.274 ± 0.009	0.271 ± 0.009	0.003 ± 0.004	1 ± 1	0.48
THC $(\mu\mathrm{M})$	132 ± 4	128 ± 4	4 ± 2	3 ± 1	0.02
$\mathrm{StO}_2\,(\%)$	70.5 ± 0.6	70.4 ± 0.6	0.2 ± 0.2	0.2 ± 0.3	0.45
$\mathrm{BFi}\,(10^{-9}\ \mathrm{cm}^2\ \mathrm{s}^{-1})$	5.2 ± 0.3	4.4 ± 0.3	0.7 ± 0.1	16 ± 2	$<10^{-3}$
$\gamma\mathrm{MRO}_2\,(10^{-10}\ \mathrm{cm}^2\ \mathrm{s}^{-1})$	2.6 ± 0.2	2.3 ± 0.2	0.35 ± 0.08	14 ± 3	$<10^{-3}$

Table B10. Table of the Pearson correlation coefficients for demographic and anatomical continuous variables. Statistically significant linear correlations are highlighted in bold.

	Age	BMI	Depth	Thickness
Age	–	**0.32**	**0.38**	−0.086
BMI	**0.32**	–	**0.69**	0.14
Depth	**0.38**	**0.69**	–	0.13
Thickness	−0.086	0.14	0.13	–

ORCID iDs

Lorenzo Cortese https://orcid.org/0000-0001-9258-0863
Pablo Fernández Esteberena https://orcid.org/0000-0003-0880-0910
Alberto Tosi https://orcid.org/0000-0003-1210-2875

References

Allen M, Poggiali D, Whitaker K, Marshall T, van Langen J and Kievit R 2021 Raincloud plots: a multi-platform tool for robust data visualization [version 2; peer review: 2 approved] *Wellcome Open Res.* **4** 63

Baker W B *et al* 2015 Pressure modulation algorithm to separate cerebral hemodynamic signals from extracerebral artifacts *Neurophotonics* **2** 1–20

Bangalore-Yogananda C-G, Rosenberry R, Soni S, Liu H, Nelson M D and Tian F 2018 Concurrent measurement of skeletal muscle blood flow during exercise with diffuse correlation spectroscopy and doppler ultrasound, Biomedical *Opt. Express* **9** 131–41

Barstow T J 2019 Understanding near infrared spectroscopy and its application to skeletal muscle research *J. Appl. Physiol.* **126** 1360–76

Basoudan N *et al* 2016 Effect of acute hypoxia on inspiratory muscle oxygenation during incremental inspiratory loading in healthy adults *Eur. J. Appl. Physiol.* **116** 841–50

Boas D A and Yodh A G 1997 Spatially varying dynamical properties of turbid media probed with diffusing temporal light correlation *J. Opt. Soc. Am.*A **14** 192–215

Bolin F P, Preuss L E, Taylor R C and Ference R J 1989 Refractive index of some mammalian tissues using a fiber optic cladding method *Appl. Opt.* **28** 2297–303

Bray F, Ferlay J, Soerjomataram I, Siegel R L, Torre L A and Jemal A 2018 Global cancer statistics 2018: GLOBOCAN estimates of incidence and mortality worldwide for 36 cancers in 185 countries *CA: Cancer J. Clin.* **68** 394–424

Buckley E M, Parthasarathy A B, Grant P E, Yodh A G and Franceschini M A 2014 Diffuse correlation spectroscopy for measurement of cerebral blood flow: future prospects *Neurophotonics* **1** 011009

Cheung C, Culver J P, Takahashi K, Greenberg J H and Yodh A G 2001 In vivo cerebrovascular measurement combining diffuse near-infrared absorption and correlation spectroscopies *Phys. Med. Biol.* **46** 2053–65

Choe R and Durduran T 2011 Diffuse optical monitoring of the neoadjuvant breast cancer therapy *IEEE J. Sel. Top. Quantum Electron.* **18** 1367–86

Ciarrocchi E and Belcari N 2017 Cerenkov luminescence imaging: physics principles and potential applications in biomedical sciences *EJNMMI Phys.* **4** 1–31

Contini D, Martelli F and Zaccanti G 1997 Photon migration through a turbid slab described by a model based on diffusion approximation: I. theory *Appl. Opt.* **36** 4587–99

Cooper D S *et al* 2009 Revised american thyroid association management guidelines for patients with thyroid nodules and differentiated thyroid cancer *Thyroid* **19** 1167–214

Cortese L *et al* 2018 Liquid phantoms for near-infrared and diffuse correlation spectroscopies with tunable optical and dynamic properties *Biomed. Opt. Express* **9** 2068–80

Cortese L *et al* 2021b Recipes for diffuse correlation spectroscopy instrument design using commonly utilized hardware based on targets for signal-to-noise ratio and precision, Biomedical *Optics Express* **12** 3265–81

Cortese L, Zanoletti M, Karadeniz U, Pagliazzi M, Yaqub M A, Busch D R, Mesquida J and Durduran T 2021c Performance assessment of a commercial continuous-wave near-infrared spectroscopy tissue oximeter for suitability for use in an international, multi-center clinical trial *Sensors* **21** 6957

Cortese L *et al* 2021a The LUCA device: a multi-modal platform combining diffuse optics and ultrasound imaging for thyroid cancer screening, biomedical *Opt. Express* **12** 3392–409
Cortese L *et al* 2023 DATA SET: *In vivo* characterization of the optical and hemodynamic properties of the human sternocleidomastoid muscle through ultrasound-guided hybrid near-infrared spectroscopies *Zenodo* (https://doi.org/10.5281/zenodo.7741369)
Culver J P, Durduran T, Furuya D, Cheung C, Greenberg J H and Yodh A G 2003 Diffuse optical tomography of cerebral blood flow, oxygenation, and metabolism in rat during focal ischemia *J. Cereb. Blood Flow Metab.* **23** 911–24
DAndrea C, Spinelli L, Bassi A, Giusto A, Contini D, Swartling J, Torricelli A and Cubeddu R 2006 Time-resolved spectrally constrained method for the quantification of chromophore concentrations and scattering parameters in diffusing media *Opt. Express* **14** 1888–98
Delpy D T, Cope M, van der Zee P, Arridge S, Wray S and Wyatt J 1988 Estimation of optical pathlength through tissue from direct time of flight measurement *Phys. Med. Biol.* **33** 1433–42
Di Sieno L *et al* 2019 Systematic study of the effect of ultrasound gel on the performances of time-domain diffuse optics and diffuse correlation spectroscopy *Biomed. Opt. Express* **10** 3899–915
Dres M, Dubé B-P, Mayaux J, Delemazure J, Reuter D, Brochard L, Similowski T and Demoule A 2017 Coexistence and impact of limb muscle and diaphragm weakness at time of liberation from mechanical ventilation in medical intensive care unit patients *Am. J. Respiratory Crit. Care Med.* **195** 57–66
Dres M, Dubé B-P, Goligher E, Vorona S, Demiri S, Morawiec E, Mayaux J, Brochard L, Similowski T and Demoule A 2020 Usefulness of parasternal intercostal muscle ultrasound during weaning from mechanical ventilation *Anesthesiology* **132** 1114–25
Dres M and Demoule A 2018 Diaphragm dysfunction during weaning from mechanical ventilation: an underestimated phenomenon with clinical implications *Crit. Care* **22** 1–8
Durduran T, Choe R, Baker W B and Yodh A G 2010 Diffuse optics for tissue monitoring and tomography *Rep. Prog. Phys.* **73** 076701
Durduran T, Choe R, Culver J P, Zubkov L, Holboke M J, Giammarco J, Chance B and Yodh A G 2002 Bulk optical properties of healthy female breast tissue *Phys. Med. Biol.* **47** 2847–61
Durduran T and Yodh A G 2014 NeuroImage Diffuse correlation spectroscopy for non-invasive , micro-vascular cerebral blood flow measurement *NeuroImage* **85** 51–63
Durduran T, Yu G, Burnett M G, Detre J A, Greenberg J H, Wang J, Zhou C and Yodh A G 2004 Diffuse optical measurement of blood flow, blood oxygenation, and metabolism in a human brain during sensorimotor cortex activation *Opt. Lett.* **29** 1766–8
Fang Q 2010 Mesh-based monte carlo method using fast ray-tracing in plücker coordinates, Biomedical *Optics Express* **1** 165–75
Farzam P, Lindner C, Weigel U M, Suarez M, Urbano-Ispizua A and Durduran T 2014 Noninvasive characterization of the healthy human manubrium using diffuse optical spectroscopies *Physiol. Meas.* **35** 1469–91
Ferrari M, Mottola L and Quaresima V 2004 Principles, techniques, and limitations of near infrared spectroscopy *Can. J. Appl. Physiol.* **29** 463–87
Field S, Kelly S and Macklem P 1982 The oxygen cost of breathing in patients with cardiorespiratory disease *Am. Rev. Respiratory Dis.* **126** 9–13
Funk G-C *et al* 2010 Incidence and outcome of weaning from mechanical ventilation according to new categories *Eur. Respiratory J.* **35** 88–94
Giovannella M *et al* 2019 BabyLux device: a diffuse optical system integrating diffuse correlation spectroscopy and time-resolved near-infrared spectroscopy for the neuromonitoring of the premature newborn brain *Neurophotonics* **6** 025007.1–025007.15
Giovannella M, Urtane E, Zanoletti M, Karadeniz U, Rubins U, Weigel U M, Marcinkevics Z and Durduran T 2021 Microvascular blood flow changes of the abductor pollicis brevis muscle during sustained static exercise *Biomed. Opt. Express* **12** 4235–48
Gómez C A, Boas D, Reid W D and Roblyer D 2023 A combined frequency domain diffuse optical spectroscopy and diffuse correlation spectroscopy system towards inspiratory muscle metabolism monitoring of mechanically ventilated patients *Proc. SPIE, Multiscale Imaging and Spectroscopy IV* ed P J Campagnola, D M Roblyer and A J Walsh (SPIE: International Society for Optics and Photonics) vol PC12363PC123630J (https://doi.org/10.1117/12.2650686)
Gray H and Carter H 1901 *Gray›s Anatomy* (US: Barnes & Noble Books)
Gruartmoner G, Mesquida J, Masip J, Martínez M L, Villagra A, Baigorri F, Pinsky M R and Artigas A 2014 Thenar oxygen saturation during weaning from mechanical ventilation: an observational study *Eur. Respiratory J.* **43** 213–20
Guenette J A, Henderson W R, Dominelli P B, Querido J S, Brasher P M, Griesdale D E, Boushel R and Sheel A W 2011 Blood flow index using near-infrared spectroscopy and indocyanine green as a minimally invasive tool to assess respiratory muscle blood flow in humans *Am. J. Physiol.-Regulatory, Integrat. Comparative Physiol.* **300** R984–92
Gurley K, Shang Y and Yu G 2012 Noninvasive optical quantification of absolute blood flow, blood oxygenation, and oxygen consumption rate in exercising skeletal muscle *J. Biomed. Opt.* **17** 075010
Haskell R C, Svaasand L O, Tsay T-T, Feng T-C, Tromberg B J and McAdams M S 1994 Boundary conditions for the diffusion equation in radiative transfer *J. Opt. Soc. Am.*A **11** 2727–41
Haugen B R *et al* 2016 2015 American thyroid association management guidelines for adult patients with thyroid nodules and differentiated thyroid cancer: the Aamerican thyroid association guidelines task force on thyroid nodules and differentiated thyroid cancer *Thyroid* **26** 1–133
He L *et al* 2018 Noninvasive continuous optical monitoring of absolute cerebral blood flow in critically ill adults *Neurophotonics* **5** 1–15
Hegedüs L 2004 The thyroid nodule *New Engl. J. Med.* **351** 1764–71
Hyttel-Sorensen S, Sorensen L C, Riera J and Greisen G 2011 Tissue oximetry: a comparison of mean values of regional tissue saturation, reproducibility and dynamic range of four nirs-instruments on the human forearm, Biomedical *Opt. Express* **2** 3047–57
Istfan R, Gómez C A, Applegate M, Rozenberg D, Reid W D and Roblyer D 2021 Hemodynamics of the sternocleidomastoid measured with frequency domain near-infrared spectroscopy towards non-invasive monitoring during mechanical ventilation, Biomedical *Opt. Express* **12** 4147–62
Jermyn M, Ghadyani H R, Mastanduno M A, Turner W D, Davis S C, Dehghani H and Pogue B W 2013 Fast segmentation and high-quality three-dimensional volume mesh creation from medical images for diffuse optical tomography *J. Biomed. Opt.* **18** 086007
Karlas A *et al* 2021 Multispectral optoacoustic tomography of peripheral arterial disease based on muscle hemoglobin gradients - a pilot clinical study *Ann. Transl. Med.* **9** 36
Katayama K, Suzuki Y, Hoshikawa M, Ohya T, Oriishi M, Itoh Y and Ishida K 2015 Hypoxia exaggerates inspiratory accessory muscle deoxygenation during hyperpnoea *Respir. Physiol. Neurobiol.* **211** 1–8
Kleiser S, Nasseri N, Andresen B, Greisen G and Wolf M 2016 Comparison of tissue oximeters on a liquid phantom with adjustable optical properties, Biomedical *Opt. Express* **7** 2973–92
Kleiser S, Ostojic D, Andresen B, Nasseri N, Isler H, Scholkmann F, Karen T, Greisen G and Wolf M 2018 Comparison of tissue oximeters on a liquid phantom with adjustable optical properties: an extension *Biomed. Opt. Express* **9** 86–101
Knief U and Forstmeier W 2021 Violating the normality assumption may be the lesser of two evils *Behav. Res. Methods* **53** 2576–90

Kwong N *et al* 2015 The influence of patient age on thyroid nodule formation, multinodularity, and thyroid cancer risk *J. Clin. Endocrinol. Metab.* **100** 4434–40
Lanka P *et al* 2022 Multi-laboratory performance assessment of diffuse optics instruments: the BitMap exercise *J. Biomed. Opt.* **27** 074716
Larimer J L 1959 Hemoglobin concentration and oxygen capacity of mammalian blood *J. Elisha Mitchell Sci. Soc.* **75** 174–7
Li Z, Baker W B, Parthasarathy A B, Ko T S, Wang D, Schenkel S, Durduran T, Li G and Yodh A G 2015 Calibration of diffuse correlation spectroscopy blood flow index with venous-occlusion diffuse optical spectroscopy in skeletal muscle *J. Biomed. Opt.* **20** 125005
Lindner C 2017 Translation of non-invasive optical measurements of hemodynamics and oxygen metabolism to the clinic *PhD Thesis* ICFO - The Institute of Photonic Sciences
Lindner C, Mora M, Farzam P, Squarcia M, Johansson J, Weigel U M, Halperin I, Hanzu F A and Durduran T 2016 Diffuse optical characterization of the healthy human thyroid tissue and two pathological case studies *PLoS One* **11** e0147851
Martelli F 2009 *Light Propagation Through Biological Tissue and Other Diffusive Media: Theory, Solutions, and Software* (SPIE Press)
Mesquida J, Gruartmoner G, Espinal C, Masip J, Sabatier C, Villagrá A, Gømez H, Pinsky M, Baigorri F and Artigas A 2020 Thenar oxygen saturation (StO_2) alterations during a spontaneous breathing trial predict extubation failure *Ann. Intensive Care* **10** 1–7
Meade M, Guyatt G, Cook D, Griffith L, Sinuff T, Kergl C, Mancebo J, Esteban A and Epstein S 2001 Predicting success in weaning from mechanical ventilation *Chest* **120** 400S–424S
Mesquita R C *et al* 2013 Influence of probe pressure on the diffuse correlation spectroscopy blood flow signal: extra-cerebral contributions *Biomed. Opt. Express* **4** 978–94
Milej D, Shahid M, Abdalmalak A, Rajaram A, Diop M and Lawrence K S 2020 Characterizing dynamic cerebral vascular reactivity using a hybrid system combining time-resolved near-infrared and diffuse correlation spectroscopy *Biomed. Opt. Express* **11** 4571–85
Mourant J R, Fuselier T, Boyer J, Johnson T M and Bigio I J 1997 Predictions and measurements of scattering and absorption over broad wavelength ranges in tissue phantoms *Appl. Opt.* **36** 949–57
Murkin J M and Arango M 2009 Near-infrared spectroscopy as an index of brain and tissue oxygenation *Br. J. Anaesthesia* **103** i3–13
Murphy W G 2014 The sex difference in haemoglobin levels in adultsmechanisms, causes, and consequences *Blood Rev.* **28** 41–7
Nasseri N, Kleiser S, Ostojic D, Karen T and Wolf M 2016 Quantifying the effect of adipose tissue in muscle oximetry by near infrared spectroscopy, Biomedical *Opt. Express* **7** 4605–19
Parthasarathy S, Jubran A, Laghi F and Tobin M J 2007 Sternomastoid, rib cage, and expiratory muscle activity during weaning failure *J. Appl. Physiol.* **103** 140–7
Patterson M S, Chance B and Wilson B C 1989 Time resolved reflectance and transmittance for the non- invasive measurement of tissue optical properties *Appl. Opt.* **28** 2331–6
Perrey S and Ferrari M 2018 Muscle oximetry in sports science: a systematic review *Sports Med.* **48** 597–616
Pifferi A, Contini D, Dalla Mora A, Farina A, Spinelli L and Torricelli A 2016 New frontiers in time-domain diffuse optics, a review *J. Biomed. Opt.* **21** 091310
Pifferi A, Torricelli A, Cubeddu R, Quarto G, Re R, Sekar S K, Spinelli L, Farina A, Martelli F and Wabnitz H 2015 Mechanically switchable solid inhomogeneous phantom for performance tests in diffuse imaging and spectroscopy *J. Biomed. Opt.* **20** 121304
Pifferi A *et al* 2005 Performance assessment of photon migration instruments: the medphot protocol *Appl. Opt.* **44** 2104–14
Pirovano I, Porcelli S, Re R, Spinelli L, Contini D, Marzorati M and Torricelli A 2021 Effect of adipose tissue thickness and tissue optical properties on the differential pathlength factor estimation for nirs studies on human skeletal muscle, Biomedical *Opt. Express* **12** 571–87
Pogue B W, Poplack S P, McBride T O, Wells W A, Osterman K S, Osterberg U L and Paulsen K D 2001 Quantitative hemoglobin tomography with diffuse near-infrared spectroscopy: pilot results in the breast *Radiology* **218** 261–6
Quaresima V, Farzam P, Anderson P, Farzam P Y, Wiese D, Carp S A, Ferrari M and Franceschini M A 2019 Diffuse correlation spectroscopy and frequency-domain near-infrared spectroscopy for measuring microvascular blood flow in dynamically exercising human muscles *J. Appl. Physiol.* **127** 1328–37
Reid W D *et al* 2016 Recruitment and deoxygenation of selected respiratory and skeletal muscles during incremental loading in stable COPD patients *J. Cardiopulmonary Rehabil. Prevention* **36** 279–87
Renna M, Buttafava M, Behera A, Zanoletti M, Di Sieno L, Dalla Mora A, Contini D and Tosi A 2019 Eight-wavelength, dual detection channel instrument for near-infrared time-resolved diffuse optical spectroscopy *IEEE J. Sel. Topics Quantum Electron.* **25** 1–11
Roche-Labarbe N, Carp S A, Surova A, Patel M, Boas D A, Grant P E and Franceschini M A 2010 Noninvasive optical measures of CBV, StO_2, CBF index, and $rCMRO_2$ in human premature neonates brains in the first six weeks of life *Human Brain Mapping* **31** 341–52
Roche-Labarbe N, Fenoglio A, Aggarwal A, Dehaes M, Carp S A, Franceschini M A and Grant P E 2012 Near-infrared spectroscopy assessment of cerebral oxygen metabolism in the developing premature brain *J. Cereb. Blood Flow Metab.* **32** 481–8
Rodrigues A, Louvaris Z, Dacha S, Janssens W, Pitta F, Vogiatzis I, Gosselink R and Langer D 2020 Differences in respiratory muscle responses to hyperpnea or loaded breathing in copd *Med. Sci. Sports Exercise* **52** 1126–34
Roussos C *et al* 1982 The respiratory muscles *N. Engl. J. Med.* **307** 786–97
Schielzeth H, Dingemanse N J, Nakagawa S, Westneat D F, Allegue H, Teplitsky C, Réale D, Dochtermann N A, Zsolt Garamszegi L and Araya-Ajoy Y G 2020 Robustness of linear mixed-effects models to violations of distributional assumptions *Methods Ecology Evolution* **11** 1141–52
Shadgan B, Guenette J A, Sheel A W and Reid W D 2011 Sternocleidomastoid muscle deoxygenation in response to incremental inspiratory threshold loading measured by near infrared spectroscopy *Respiratory Physiol. Neurobiol.* **178** 202–9
Shang Y, Gurley K and Yu G 2013 Diffuse correlation spectroscopy (dcs) for assessment of tissue blood flow in skeletal muscle: recent progress *Anat. Physiol.: Curr. Res.* **3** 128
Spinelli L, Torricelli A, Pifferi A, Taroni P, Danesini G M and Cubeddu R 2004 Bulk optical properties and tissue components in the female breast from multiwavelength time-resolved optical mammography *J. Biomed. Opt.* **9** 1137–42
Srinivasan S, Pogue B W, Jiang S, Dehghani H, Kogel C, Soho S, Gibson J J, Tosteson T D, Poplack S P and Paulsen K D 2003 Interpreting hemoglobin and water concentration, oxygen saturation, and scattering measured in vivo by near-infrared breast tomography *Proc. Natl Acad. Sci.* **100** 12349–54
Tanaka T, Basoudan N, Melo L T, Wickerson L, Brochard L J, Goligher E C and Reid W D 2018 Deoxygenation of inspiratory muscles during cycling, hyperpnoea and loaded breathing in health and disease: a systematic review *Clin. Physiol. Functional Imaging* **38** 554–65
Torricelli A, Contini D, Pifferi A, Caffini M, Re R, Zucchelli L and Spinelli L 2014 Time domain functional NIRS imaging for human brain mapping *Neuroimage* **85** 28–50
Van Hollebeke M, Poddighe D, Clerckx B, Muller J, Hermans G, Gosselink R, Langer D and Louvaris Z 2022 High-intensity inspiratory muscle training improves scalene and sternocleidomastoid muscle oxygenation parameters in patients with weaning difficulties: A randomized controlled trial *Front. Physiol.* **13** 786575

Vassilakopoulos T, Zakynthinos S and Roussos C 1996 Respiratory muscles and weaning failure *Eur. Respiratory J.* **9** 2383–400
Verdecchia K, Diop M, Lee T-Y and Lawrence K S 2013 Quantifying the cerebral metabolic rate of oxygen by combining diffuse correlation spectroscopy and time-resolved near-infrared spectroscopy *J. Biomed. Opt.* **18** 027007
Wabnitz H *et al* 2014a Performance assessment of time-domain optical brain imagers, part 1: basic instrumental performance protocol *J. Biomed. Opt.* **19** 086010
Wabnitz H *et al* 2014b Performance assessment of time-domain optical brain imagers, part 2: nEUROPt protocol *J. Biomed. Opt.* **19** 086012
Wagner A L *et al* 2021 Precision of handheld multispectral optoacoustic tomography for muscle imaging *Photoacoustics* **21** 100220
Wang L *et al* 2022 Non-invasive monitoring of blood oxygenation in human placentas via concurrent diffuse optical spectroscopy and ultrasound imaging *Nat. Biomed. Eng.* **6** 1017–30
Wolf M, Ferrari M and Quaresima V 2007 Progress of near-infrared spectroscopy and topography for brain and muscle clinical applications *J. Biomed. Opt.* **12** 062104
Yamada Y, Suzuki H and Yamashita Y 2019 Time-domain near-infrared spectroscopy and imaging: a review *Appl. Sci.* **9** 1127
Yang C-C, Yang P-C, Chen J-J J, Lai Y-H, Hu C-H, Chang Y, Tu S J and Guo L-Y 2020a Near-infrared spectroscopy for monitoring sternocleidomastoid muscular oxygenation during isometric flexion for patients with mild nonspecific neck pain: a pilot study *Sensors* **20**
Yang J, Zhang G, Chang W, Chi Z, Shang Q, Wu M, Pan T, Huang L and Jiang H 2020b Photoacoustic imaging of hemodynamic changes in forearm skeletal muscle during cuff occlusion, Biomedical *Opt. Express* **11** 4560–70
Yu G 2012a Diffuse correlation spectroscopy (DCS): a diagnostic tool for assessing tissue blood flow in vascular-related diseases and therapies *Curr. Med. Imaging Reviews* **8** 194–210
Yu G 2012b Near-infrared diffuse correlation spectroscopy in cancer diagnosis and therapy monitoring *J. Biomed. Opt.* **17** 010901
Yu G, Durduran T, Lech G, Zhou C, Chance B, Mohler E R and Yodh A G 2005 Time-dependent blood flow and oxygenation in human skeletal muscles measured with noninvasive near-infrared diffuse optical spectroscopies *J. Biomed. Opt.* **10** 024027
Yu G, Floyd T F, Durduran T, Zhou C, Wang J, Detre J A and Yodh A G 2007 Validation of diffuse correlation spectroscopy for muscle blood flow with concurrent arterial spin labeled perfusion MRI *Opt. Express* **15** 1064–75
Zhou C *et al* 2007 Diffuse optical monitoring of blood flow and oxygenation in human breast cancer during early stages of neoadjuvant chemotherapy *J. Biomed. Opt.* **12** 051903